The Astrophysical Journal, 968:38 (17pp), 2024 June 10 https://doi.org/10.3847/1538-4357/ad4265


# A Census of Photometrically Selected Little Red Dots at $4 < z < 9$ in JWST Blank Fields

Vasily Kokorev[1,5], Karina I. Caputi[1,2], Jenny E. Greene[3], Pratika Dayal[1], Maxime Trebitsch[1], Sam E. Cutler[4], Seiji Fujimoto[2,5], Ivo Labbé[6], Tim B. Miller[7], Edoardo Iani[1], Rafael Navarro-Carrera[1], and Pierluigi Rinaldi[1]
[1] Kapteyn Astronomical Institute, University of Groningen, 9700 AV Groningen, The Netherlands; vkokorev@utexas.edu
[2] Cosmic Dawn Center (DAWN), Niels Bohr Institute, University of Copenhagen, Jagtvej 128, København N, DK-2200, Denmark
[3] Department of Astrophysical Sciences, Princeton University, 4 Ivy Lane, Princeton, NJ 08544, USA
[4] Department of Astronomy, University of Massachusetts, Amherst, MA 01003, USA
[5] Department of Astronomy, The University of Texas at Austin, Austin, TX 78712, USA
[6] Centre for Astrophysics and Supercomputing, Swinburne University of Technology, Melbourne, VIC 3122, Australia
[7] Center for Interdisciplinary Exploration and Research in Astrophysics (CIERA), Northwestern University, 1800 Sherman Ave, Evanston, IL 60201, USA
*Received 2024 January 23; revised 2024 April 6; accepted 2024 April 14; published 2024 June 6*

## Abstract

Observations with the James Webb Space Telescope (JWST) have uncovered numerous faint active galactic nuclei (AGN) at $z \sim 5$ and beyond. These objects are key to our understanding of the formation of supermassive black holes (SMBHs), their coevolution with host galaxies, as well as the role of AGN in cosmic reionization. Using photometric colors and size measurements, we perform a search for compact red objects in an array of blank deep JWST/NIRCam fields totaling $\sim$640 arcmin$^2$. Our careful selection yields 260 reddened AGN candidates at $4 < z_{\rm phot} < 9$, dominated by a point-source-like central component ($\langle r_{\rm eff} \rangle < 130$ pc) and displaying a dichotomy in their rest-frame colors (blue UV and red optical slopes). Quasar model fitting reveals our objects to be moderately dust-extincted ($A_{\rm V} \sim 1.6$), which is reflected in their inferred bolometric luminosities of $L_{\rm bol} = 10^{44-47}$ erg s$^{-1}$ and fainter UV magnitudes $M_{\rm UV} \simeq -17$ to $-22$. Thanks to the large areas explored, we extend the existing dusty AGN luminosity functions to both fainter and brighter magnitudes, estimating their number densities to be $\times$100 higher than for UV-selected quasars of similar magnitudes. At the same time, they constitute only a small fraction of all UV-selected galaxies at similar redshifts, but this percentage rises to $\sim$10% for $M_{\rm UV} \sim -22$ at $z \sim 7$. Finally, assuming a conservative case of accretion at the Eddington rate, we place a lower limit on the SMBH mass function at $z \sim 5$, finding it to be consistent with both theory and previous JWST observations.

*Unified Astronomy Thesaurus concepts:* Galaxies (573); High-redshift galaxies (734); Active galaxies (17); Active galactic nuclei (16)

## 1. Introduction

The remarkable sensitivity and angular resolution of the James Webb Space Telescope (JWST) at infrared wavelengths is enabling us to explore the distant Universe like never before. This allows for an exceptionally detailed examination of the characteristics of known high-$z$ sources (e.g., Bunker et al. 2023; Maiolino et al. 2023) and, at the same time, reveals the presence of more and farther galaxies (e.g., Naidu et al. 2022; Adams et al. 2023; Atek et al. 2023; Austin et al. 2023; Bradley et al. 2023; Finkelstein et al. 2023; Robertson et al. 2023; Casey et al. 2024), some of them spectroscopically confirmed beyond $z > 13$ (Curtis-Lake et al. 2023; Wang et al. 2023).

What truly tests our models and preconceived vision of galaxy evolution is not how early we can see these objects, but the questions they raise regarding the balance between their mass, UV luminosity, and age. The excess of high-$z$ galaxies at the bright end ($M_{\rm UV} \leqslant -20$) of the UV luminosity function (UVLF) is in tension with current theoretical frameworks (Behroozi & Silk 2015; Dayal et al. 2017; Behroozi et al. 2019, 2020; Davé et al. 2019; Yung et al. 2019, 2020; Wilkins et al. 2022; Kannan et al. 2023; Mason et al. 2023; Mauerhofer & Dayal 2023), which suggests exotic IMFs, little to no dust attenuation, or a higher than anticipated density of galaxies undergoing active galactic nuclei (AGN) phenomena (e.g., Finkelstein & Bagley 2022; Pacucci et al. 2022; Boylan-Kolchin 2023; Ferrara et al. 2023; Fujimoto et al. 2023c; Lovell et al. 2023; Steinhardt et al. 2023; Sun et al. 2023).

Although early hints also existed in prior works (Morishita et al. 2020; Fujimoto et al. 2022; Endsley et al. 2023), one of the most intriguing discoveries from early JWST imaging is that of compact red sources with a "$v$-shaped" spectral energy distribution (SED)—namely, a blue UV continuum and a steep red slope in the rest-frame optical (Furtak et al. 2023a; Labbé et al. 2023a, 2023b). While the first photometric selections of these objects included spatially resolved targets that could be early massive compact galaxies (Barro et al. 2024), spectra revealed clear evidence for broad H$\alpha$ and/or H$\beta$ emission indicative of actively accreting supermassive black holes (SMBHs; Fujimoto et al. 2023c; Killi et al. 2023; Kocevski et al. 2023; Kokorev et al. 2023a; Übler et al. 2023; Furtak et al. 2024; Greene et al. 2024; Matthee et al. 2024).

Dubbed "little red dots" (LRDs), these sources have SEDs characterized by a unique "$v$-shaped" continuum combined with their point-source morphology (Furtak et al. 2023a; Labbé et al. 2023a, 2023b). However, what truly makes the LRDs stand out is their high number densities. It appears that LRDs may account for a few percent of the galaxy population at $z > 5$ and are far more numerous than the lowest-luminosity known UV-selected quasars. Likewise, they appear to account for $\sim$20% of broadline (BL)–selected AGN at $z \sim 5$–6 (Harikane et al. 2023; Labbé et al. 2023a; Greene et al. 2024; Maiolino et al. 2024), which is higher than the fraction of dusty red quasars at $z < 2$ (Banerji et al. 2015; Glikman et al. 2015). These red dots are generally observed at $z \sim 5$ (Labbé et al. 2023a), but can potentially be

**Table 1**
Properties of the Observed Fields with JWST/NIRCam Observations

| Field | R.A. (deg) | Decl. (deg) | Science Area (arcmin$^2$) | NIRCam Depths (mag) |
|---|---|---|---|---|
| CEERS | 214.920 | 52.870 | 97.0 | 28.8/28.5/28.7/28.9/29.0/28.4 |
| PRIMER-COSMOS | 150.119 | 2.325 | 197.2 | 27.9/28.1/28.3/28.7/28.6/28.2 |
| PRIMER-UDS | 34.372 | −5.210 | 274.6 | 27.6/27.8/28.0/28.3/28.4/28.0 |
| GOODS-S | 53.142 | −27.798 | 69.7 | 29.6/29.6/29.5/29.8/29.6/29.3 |

**Note.** NIRCam depths: expressed as $5\sigma$ within the $0\farcs36$ apertures used for the photometric extraction in the area covered by F115W/F150W/F200W/F277W/F356W/F444W.

found even at $z > 9$ (Leung et al. 2023). However, these initial LRD studies were performed with limited spectroscopic samples and/or small areas of the sky, covering only ∼20–40 arcmin$^2$. The numbers of compact red objects could therefore be further affected by cosmic variance, which makes it quite difficult to assess their real importance and diversity.

Extending the selection of this compact red population of low-luminosity BL AGN candidates to larger areas would thus be necessary to study their complete demographics, limiting the effects of cosmic variance. In addition, this would provide us with a sufficient level of detail toward a better understanding of the total number densities of obscured AGN at high-$z$ as well as the potential role that these sources play in cosmic reionization (e.g., see Grazian et al. 2018; Mitra et al. 2018; Dayal et al. 2020, 2024; Trebitsch et al. 2023).

In this work, we present a carefully selected sample of 260 reddened AGN candidates in the ∼640 arcmin$^2$ area covering some of the deepest blank extragalactic JWST fields. Examining such a large area will ensure that we are reducing the effects of cosmic variance to a minimum, while our focus on blank fields lessens the selection biases and avoids volume uncertainties arising from lensing magnification.

Throughout this work, we assume a flat ΛCDM cosmology (e.g., Planck Collaboration et al. 2020), with $\Omega_{m,0} = 0.3$, $\Omega_{\Lambda,0} = 0.7$, and $H_0 = 70\,\mathrm{km\,s^{-1}\,Mpc^{-1}}$, and a Chabrier (2003) initial mass function (IMF) between 0.1 and 100 $M_\odot$. All magnitudes are expressed in the AB system (Oke 1974).

## 2. Observations and Data

In this work, we use JWST data from the following programs/fields—CEERS (# 1345; PI: S. Finkelstein; Bagley et al. 2023) in the Extended Groth Strip (EGS), PRIMER (# 1837; PI: J. Dunlop) in COSMOS and UDS, and GOODS-S. For GOODS-S, we combine the available data from multiple broad- and medium-band programs—FRESCO (# 1895; PI: P. Oesch; Oesch et al. 2023), JADES (# 1180, 1210, 1286, and 1287; PIs: D. Eisenstein and N. Luetzgendorf; Eisenstein et al. 2023a, 2023b), and JEMS (# 1963; PI: C. Williams; Williams et al. 2023b). We provide a general overview of these four fields in Table 1. More detailed information—including specific filters, depths, and survey designs—can be found in the overview papers for each data release.

### 2.1. JWST Imaging Data Reduction

We homogeneously processed all the publicly available JWST imaging obtained with the NIRCam and MIRI in a variety of public JWST fields, presented in Table 1. The images have all been reduced with the GRIZLI pipeline (Brammer 2023), using the `jwst_1084.pmap`, and follow the same methodology of (multiple) previous studies (e.g., Jin et al. 2023; Kokorev et al. 2023b; Valentino et al. 2023). Compared to the standard pipeline, we incorporate additional corrections to account for cosmic rays and stray light (see, e.g., Bradley et al. 2023), $1/f$ noise, detector-level artifacts ("wisps" and "snowballs"), and bias in individual exposures (see, e.g., Rigby et al. 2023). For the PRIMER data, we introduce an additional procedure that alleviates the detrimental effects of the diagonal striping seen in some exposures, as was done in Valentino et al. (2023). Finally, our mosaics include the updated sky flats for all NIRCam filters. These reductions are publicly available as a part of the DAWN JWST Archive.[8]

These data sets are further complemented by including all available optical and near-infrared (NIR) data from the Complete Hubble Archive for Galaxy Evolution (Kokorev et al. 2022). Individual JWST and Hubble Space Telescope (HST) exposures were aligned to the same astrometric reference frame by using Gaia DR3 (Gaia Collaboration et al. 2021), then coadded and drizzled (Fruchter & Hook 2002) to a $0\farcs04$ pixel scale for all the JWST and HST filters.

Some of the fields we examine in this work have also been observed with MIRI, in one or more filters, sampling mostly the rest-frame NIR at $z \gtrsim 4$. These data, however, are not uniform in the wavelength coverage, depth, and area. In fact, only about a third of the objects in the areas we examine have public MIRI data and even fewer are actually detected. While the inclusion of the MIRI photometry can assist in further identifying the presence (or absence) of dusty, power-law-like AGN components in galaxies (e.g., see Williams et al. 2023a; Yang et al. 2023), doing so appropriately within the context of a population study requires a degree of uniformity that the current MIRI data do not possess. Therefore, we have opted to exclude MIRI photometry from our current analysis to maintain consistency across various fields.

### 2.2. Source Extraction

The initial JWST catalog was constructed by utilizing a detection image combined from all noise-weighted "wide" (W) NIRCam long-wavelength filters available, which includes F277W, F356W, and F444W. A similar detection method has already been successfully employed in several works (see, e.g., Jin et al. 2023; Kokorev et al. 2023b; Valentino et al. 2023; Weaver et al. 2024). To extract the sources and produce a segmentation map, we used SEP (Barbary 2016), a PYTHON version of SEXTRACTOR (Bertin & Arnouts 1996). Photometry was extracted in circular apertures of increasing size.

[8] dawn-cph.github.io/dja/

Correction from the aperture to the "total" values was performed by using the `flux_auto` column output of SEP, which is equivalent to the `MAG_AUTO` from SEXTRACTOR, ensuring that for each source only flux belonging to its segment is taken into account. This method has been shown to apply to both point-like and extended objects (Weaver et al. 2022, 2023), so we believe it to be adequate for our sources.

Additionally, we introduce a correction to account for the missing flux outside the Kron aperture (Kron 1980), by utilizing a method similar to the one used in Whitaker et al. (2011) and Weaver et al. (2024). In short, this procedure involves computing the fraction of the missing light outside the circularized Kron radius by analyzing curves of growth of the point-spread functions (PSFs), which were obtained empirically, by stacking stars in these various fields. This correction is then applied to the `flux_auto` values for each source. However, since our work focuses on compact (sub-NIRCam-PSF size) AGN candidates, this additional correction does not strongly influence the derived flux densities. For the same reason, we use the total fluxes, computed from $D = 0.''36$ apertures, unless specified otherwise.

## 3. Identifying Compact Red Objects

The data from CEERS, PRIMER, and various programs covering GOODS-S are well suited for a photometric search for compact obscured AGN candidates. The available HST and JWST photometry covers a complete wavelength range from 0.4 to 5 $\mu$m, in at least seven broad and medium bands, reaching a median $5\sigma$ depth of 28.3 AB mag in the F444W filter (Table 1). In our search, we explore blank fields covering a large area of $\sim$640 arcmin$^2$, which are also completely independent. In return, this will significantly limit the impact of cosmic variance and enable us to avoid dealing with the cosmic volume uncertainties introduced by the lensing magnification.

### 3.1. Color and Morphology Selection

Recently, Labbé et al. (2023a) published a large sample of photometrically identified compact red sources from the Cycle 1 JWST UNCOVER program (PIs: I. Labbé and R. Bezanson; Bezanson et al. 2022). The subsequent follow-up of 17 such objects with NIRSPec/Micro-Shutter Assembly (MSA) PRISM has resulted in a remarkable success rate of 83%, with 14 of 17 photometrically selected targets confirmed as BL AGN at $4 < z < 8.5$ (Greene et al. 2024) and 3 of 17 as brown dwarfs (Burgasser et al. 2024). In brief, the color cuts introduced in Labbé et al. (2023a) are designed to catch the break between the red continuum slope in the rest-frame optical and the blue rest-UV emission ($\lambda_{\rm rest} \sim 4000$ Å ). This color selection requires the red continuum slope to be rising in more than one adjacent filter pair, to avoid selecting galaxies with strong emission lines. Indeed, the currently available spectra of LRDs (e.g., Fujimoto et al. 2023c; Kocevski et al. 2023; Kokorev et al. 2023a; Furtak et al. 2024; Greene et al. 2024; Matthee et al. 2024) display a remarkable dichotomy in their observed spectral shapes. In particular, the SEDs at 1−2 $\mu$m (1000–2000 Å rest) are blue ($f_\lambda \propto \lambda^{-2}$) and red ($f_\lambda \propto \lambda^{0-2}$) at 3−5 $\mu$m (3100–5200 Å rest). As such, we keep the Labbé et al. (2023a) color criteria largely unchanged, only introducing some further adjustments based on the UNCOVER spectra of LRDs, namely to limit the contamination of our sample by brown dwarfs, as was suggested in Greene et al. (2024).

Colors alone would end up selecting both LRDs and extended red galaxies (see, e.g., Labbé et al. 2023a; Williams et al. 2023a, 2023b), so we introduce a further "compactness" cut to only select sources with high central flux concentration. To do that, we use the ratio between the total flux in F444W between $0.''4$ and $0.''2$ apertures. Since roughly 17% of the LRD candidates followed up with NIRSpec turned out to be brown dwarfs (Burgasser et al. 2024), we would also like to minimize the incidence of these objects in our sample. To do that, we adopt the brown dwarf removal criterion from Greene et al. (2024), based on the LRD spectra from NIRSPec/MSA. Finally, we also require our sources to be significantly ($>14\sigma$) detected in F444W and to be brighter than 27.7 AB mags, to be consistent with the UNCOVER selection. The imposed color cuts are then:

$$\begin{aligned} \texttt{red 1} = {} & \text{F115W} - \text{F150W} < 0.8 \quad \& \\ & \text{F200W} - \text{F277W} > 0.7 \quad \& \\ & \text{F200W} - \text{F356W} > 1.0, \end{aligned}$$

or

$$\begin{aligned} \texttt{red 2} = {} & \text{F150W} - \text{F200W} < 0.8 \quad \& \\ & \text{F277W} - \text{F356W} > 0.6 \quad \& \\ & \text{F277W} - \text{F444W} > 0.7, \end{aligned}$$

which are effectively selecting our low- ($z < 6$) and high- ($z > 6$) redshift samples, respectively. The compactness is given by

$$\texttt{compact} = f_{\rm f444w}(0.''4)/f_{\rm f444w}(0.''2) < 1.7.$$

To limit the number of brown dwarfs in the sample, we also adopt

$$\texttt{bd\_removal} = \text{F115W} - \text{F200W} > -0.5.$$

The final selection then becomes (red 1 | red 2) & `compact` & `bd_removal`. Applying the color criteria also means that every object has to be detected ($>3\sigma$) in at least one band per color to make the selection meaningful. In the case of a nondetection, we use the $2\sigma$ upper limits, but only if the "brighter" band in the color is detected. Out of $\sim$408,000 objects covering the four fields of interest, we end up selecting 334. Most importantly, we note that no information about photometric redshifts and underlying galaxy/AGN SEDs is used at this stage, to avoid being biased by models. We discuss our photometric redshift estimate and its agreement with spec-$z$ for subsamples in the next subsection.

### 3.2. Size Measurements

While the compactness cut alone already successfully manages to select PSF-dominated point sources, we would like to provide a further fine-tuning to provide a fully quantitative rather than qualitative assessment. To do that, we fit our sources with PYSERSIC (Pasha & Miller 2023) in the F444W band. The primary goal of this is to ensure that the source is dominated by the PSF component in the reddest, least-dust-obscured band, as was done in Labbé et al. (2023a). We focus on the F444W band for this analysis, as the galactic origin of the rest-UV cannot be ruled out with current photometric (or even spectroscopic) observations. Moreover, if an object is dominated by a single star-forming region, it could appear compact in rest-UV bands, but still be extended in

the redder filters, making the F444W band the most physically constraining for our type of study.

Taking the PSF into account is imperative when measuring the sizes of unresolved objects. We generate our F444W PSFs empirically for each field by following the methodology described in Skelton et al. (2014), Whitaker et al. (2019), and Weaver et al. (2024). In brief, we identify nonsaturated stars in every field by considering objects on the stellar locus that are brighter than 24 AB mag and extract these candidates in stamps. These stamps are then centered and normalized to unity. The final PSFs are derived by averaging the weighted stamps, and they are then normalized to match the enclosed energies of the expected JWST calibration levels within 4″ diameter apertures.[9] For more details, see the appendix in Weaver et al. (2024).

The light is modeled with a single Sérsic (Sérsic 1963) profile, with the center, brightness, effective radius, Sérsic index, and axis ratio as free parameters. The prior for the index is uniform between 0.65 and 6, and the effective radius is uniform between 0.25 and 5 pixels (0.″01–0.″2). For each source, we create a 3″ square cutout (75 pixels by 75 pixels) and mask any additional sources within the stamp. Parameter values and uncertainties are calculated using the Laplace approximation, assuming that the posterior is Gaussian. We exclude fits where the resulting $\chi^2$ per pixel is greater than 2 or the best-fit flux differs from the catalog value by more than 2 AB mag. This excludes 15 sources from our sample, which by visual inspection we find are untrustworthy due to contamination from bright nearby objects.

A source can be considered to be point-like if its effective radius in the F444W band is lower than the empirical PSF FWHM (∼0.″15). It appears that our `compact` criterion is extremely effective at identifying PSF-like objects, as none of the 319 of 334 sources with reliable fits exceed a diameter of 0.″08, when considering the 95% size upper limits, corroborating the effectiveness of the compactness criterion described in Section 3. After carefully considering both colors and morphology when selecting our sample of AGN candidates, we are now able to proceed directly to the SED fitting.

### 3.3. Photometric Redshifts

To calculate photometric redshifts ($z_{\rm phot}$) for our objects, we use the PYTHON version of EAZY (Brammer et al. 2008). We choose the BLUE_SFHZ_13 model subset[10] that contains redshift-dependent star formation histories (SFHs) and dust attenuation values. More specifically, the linear combinations of log-normal SFHs included in the template set are not allowed to exceed redshifts that start earlier than the age of the Universe (for more details, see Blanton & Roweis 2007). These models are further complemented by a blue galaxy template, derived from a JWST spectrum of a $z = 8.50$ galaxy with extreme line equivalent widths (EWs; ID4590; Carnall et al. 2023).

While it might seem counterintuitive to use galaxy templates for what we believe to be AGN candidates, similar efforts presented in Labbé et al. (2023a) report a good agreement between deriving $z_{\rm phot}$ with stellar templates alone, as opposed to stellar+AGN models, finding a very good agreement between the two. This is not surprising, as when it comes to photometric redshift fitting, the key deciding factors are the positions of the Lyman (∼912 Å) and Balmer (∼4000 Å) breaks.

For the LRDs, a general absence of significant stellar contribution in the rest-frame optical (e.g., Greene et al. 2024) would result in the lack of a noticeable Balmer break, although the trough of the "*v* shape" in the rest-frame SEDs of observed LRDs is also located at roughly 4000 Å (e.g., Kokorev et al. 2023a; Furtak et al. 2024). Indeed the existence of such a feature in LRDs has resulted in their misidentification as dusty star-forming galaxies, leading to stellar mass estimates that are in tension with ΛCDM, if all the light is attributed to star formation alone (e.g., see the discussions in Boylan-Kolchin 2023; Kocevski et al. 2023; Labbé et al. 2023b; Steinhardt et al. 2023).

Spectroscopic follow-up of red compact objects hosting AGN BL emission has in fact shown a remarkable agreement between the $z_{\rm phot}$ derived with EAZY (or similar routines) and $z_{\rm spec}$. For example, in GOODS-S, Matthee et al. (2024) report an average $\sigma_z = |\Delta z|/(1+z_{\rm spec}) = 0.01$, and UNCOVER LRDs presented in Greene et al. (2024) have shown $\sigma_z \sim 0.04$. A similar consistency was also found between the initial photometric source selection and final spectra in the JADES and CEERS fields (Kocevski et al. 2023; Andika et al. 2024; Maiolino et al. 2024). As such, we consider that utilizing EAZY to derive redshifts is adequate for our sample.

We fit all the available photometry and upper limits from the HST/F435W ($\lambda_{\rm obs} \sim 0.4\,\mu$m) to JWST/F444W ($\lambda_{\rm obs} \sim 4.4\,\mu$m) filters for our sample of 319 LRDs, limiting the redshift grid between $0.01 < z < 20$. From the best-fit EAZY SEDs, we only derive photometric redshifts, delegating the estimation of the physical parameters to a different template set discussed in the next section. The uncertainties on the photometric redshift are computed from the 16th and 84th percentiles of the redshift probability distributions—$p(z)$. The availability of HST photometry allows us to securely constrain the presence of the Lyman break, either through diminishing flux, where a given filter overlaps with the break, or via upper limits, for 40% of the sources in our sample. Notably, however, the presence of the Lyman break is not required to securely constrain the redshift for high-$z$ LRDs, as the break in the optical part of the SED already places these objects in a unique color–color space, as initially shown in Labbé et al. (2023a) and then further confirmed in Greene et al. (2024). In addition, access to at least one NIRCam medium band further enhances the redshift quality by allowing us to identify the emission lines in broadband photometry. As a result, none of our objects have double-peaked redshift solutions. Despite that, since our sample is still only identified photometrically, appropriately taking into account $z_{\rm phot}$ uncertainties is crucial when deriving the physical parameters and luminosity functions in the upcoming sections.

### 3.4. Quasar Template Fitting

While the origin of the rest-frame UV light in LRDs remains elusive, growing samples of JWST spectra consistently show either a complete absence of or a lack of a significant contribution from the host galaxy to the total flux in the rest-frame optical ($\lambda_{\rm obs} \gtrsim 2\,\mu$m; Kokorev et al. 2023a; Furtak et al. 2024; Greene et al. 2024). This is generally evidenced by comparing the expected $L_{5100}$ from broad Balmer series lines

[9] https://jwst-docs.stsci.edu/jwst-near-infrared-camera/nircam-performance/nircam-point-spread-functions

[10] https://github.com/gbrammer/eazy-photoz/tree/master/templates/sfhz

(generally Hβ and/or Hα) to the observed values. For example, Greene et al. (2024) find that Hα-derived and observed $L_{5100}$ agree within a factor of 2 for the objects that have Hα PRISM coverage. Supporting this, Furtak et al. (2024) and Kokorev et al. (2023a) also find that BH masses ($M_{\rm BH}$) derived via broad Hβ line luminosities and continua are identical, given the scatter of the relations derived from AGN reverberation mapping (see, e.g., Kaspi et al. 2000; Greene & Ho 2005), hinting at negligible stellar components. Furthermore, none of the currently known spectroscopically confirmed LRDs in A2744 are detected by the Atacama Large Millimeter/submillimeter Array (ALMA) at 1.2 mm down to $<70$ μJy ($2\sigma$), which strongly limits the contribution of obscured star formation (see, e.g., Labbé et al. 2013, 2023a), unless the dust is either very cold, very hot, or diffuse. Indeed, when both JWST data and ALMA upper limits (Fujimoto et al. 2023a, 2023b) are considered in a joint AGN+galaxy template fitting for the objects described in Kokorev et al. (2023a) and Furtak et al. (2024), the contribution of the galaxy model to the total rest-frame optical light is negligible. Finally, robust measurements of effective radii for all UNCOVER LRDs, while also taking into account the empirically derived PSFs (see Weaver et al. 2024), find no strong evidence for extended emission associated with the host galaxy in the F444W band.

Unfortunately, a lack of deep and uniform ALMA coverage for our objects prevents us from carrying out joint AGN +galaxy template fitting to ascertain the amount of AGN contribution to the optical SED. While it is possible to do it with only JWST photometry, such a fit would be too degenerate, given the available number of bands and the number of models required. However, the objects in our work were specifically selected with the color and compactness criteria largely mirroring those used to identify BL AGN in UNCOVER. It is reasonable therefore to assume that given similarly red ($f_\lambda \propto \lambda^{0-2}$ at 3100–5200 Å rest) slopes, the rest-optical continuum in our sources is also dominated by AGN light.

In terms of luminosity, the dust-obscured component is dominating the light from LRDs and must be substantially attenuated ($A_{\rm V} \sim 1$–2) in order to fit the observed red slope. Given that, the rest-UV light should not be visible at all ($A_{\rm UV} > 10$). From our photometry, however, we see that while the blue component is weak (only a few percent of the red component), it is not reddened. This emission can be interpreted as either scattered light from the AGN itself or the host galaxy (see the discussions in Labbé et al. 2023a; Greene et al. 2024). However, even when spectra are available (Greene et al. 2024), given the similarities between the UV slopes of quasars and young star-forming galaxies, these two models are equally good representations of the observed light. Our available data also do not allow us to make a clear distinction between these two possibilities, therefore, to avoid overinterpreting the origins of the rest-UV emission, we will assume the scattered-light-only (unreddened) template in our modeling. We caution the reader that as a result of the unknown origin of the blue light, the rest-UV properties derived in this paper do not necessarily represent the physical conditions of the potential AGN our LRDs might host. Due to the aforementioned similarity between the UV slopes in quasars and SFGs, the $M_{\rm UV}$ values derived from both galaxy and quasar fits are thus nearly identical.

Following the galaxy-only fits presented in Section 3.3 and keeping the above considerations in mind, we now would like to explore an AGN-only scenario, where we model the observed light with a two-component AGN model. The first one is the empirical model based on a composite of 2200 Sloan Digital Sky Survey (SDSS) quasar spectra (Vanden Berk et al. 2001), and the second is derived from 27 NIR quasar spectra of Glikman et al. (2006). We then combine and renormalize both templates, allowing us to cover the full range from rest-UV to the NIR.

The same approach has already been successfully employed in Labbé et al. (2023a) for a photometrically selected sample of red dots, and then later for PRISM spectra of 14 such objects in Greene et al. (2024) and Kokorev et al. (2023a). We fit the unreddened AGN component together with the Small Magellanic Cloud law (Gordon et al. 2003) attenuated ($A_{\rm V} = 0.1$–4) version of the same composite template. With the photometric redshift being fixed, we are fitting for a total of three free parameters.

We find the AGN-only fits to be a marginally better representation of the observed photometry, when compared to galaxy-only EAZY fits, with $\langle \chi^2_\nu \rangle = 3.0^{+3.7}_{-1.8}$ for the former and $\langle \chi^2_\nu \rangle = 4.2^{+6.6}_{-1.9}$ for the latter, with a difference of approximately $\langle \Delta\chi^2_\nu \rangle \sim 1$. Similar findings were also presented in Labbé et al. (2023a), even without ALMA photometry, and Barro et al. (2024), where no significant $\chi^2$ difference exists between dusty star formation and reddened AGN models.

### 3.5. Extreme EW of Emission Lines

Before focusing on the final sample of reddened AGN candidates, we would like to conduct one final test that concerns the potential presence of strong emission lines, particularly Hα in the spectra of LRDs. The empirical quasar templates presented in Vanden Berk et al. (2001), which we used to fit our objects, generally contain bright AGN with a rest-frame Hα EW ∼ 190 Å. Conversely, the recent literature results that analyze LRD spectra (Killi et al. 2023; Matthee et al. 2024) have found that the EW of Hα can reach and even exceed 500 Å. Such strong emission lines can contribute to the flux observed in the medium- and even broadband JWST filters in a non-negligible way, making the observed colors redder. In return, if such strong emission lines are not present in the templates, the value of the $A_{\rm V}$, and subsequently other physical properties dependent on it (e.g., $L_{\rm bol}$), can be overestimated.

To test the significance of this effect, we do the following. Starting with the original combined Vanden Berk et al. (2001) and Glikman et al. (2006) template sets, we isolate the regions that cover the Hβ+[O III] and Hα lines and use a spline function to fit the continuum, while masking out the regions containing line complexes. While doing this, we successfully verify that the measured rest-frame EW of these lines is exactly as the one reported in Vanden Berk et al. (2001). Finally, we uniformly boost the continuum-subtracted spectrum to a point where the EW of the Hα line measures at ∼500 Å, and add back the continuum. We then refit all of our sources, following the same considerations as described in Section 3.4.

Using models with boosted emission-line strengths, we indeed find the best-fit $A_{\rm V}$ values to be systematically lower, albeit only by ∼0.1 mag, on average, compared to the original templates. This offset is well within our quoted uncertainty on

the $A_V$ from the SED fitting. We thus conclude that even if some of our AGN candidates indeed contained very high-EW H$\alpha$ emission lines, the physical properties derived with the original Vanden Berk et al. (2001) template set should still remain valid. Despite being small, this offset is systematic, so we still incorporate it into our uncertainties when computing the number densities in the subsequent sections.

### 3.6. Final Sample of LRDs

Following the initial object selection and SED fitting, we are now in a position to define our final sample of LRDs. The primary goal of this work is to explore the photometrically selected dusty AGN candidates in the high-$z$ Universe, compare these results to robust samples of spectroscopically identified BL AGN, and potentially extend these examinations to fainter UV magnitudes and bolometric luminosities. The accurate determination of these parameters is contingent upon good coverage of the spectral break between the blue and red components at ∼4000 Å. This is crucial to confirm that the selected objects indeed exhibit the characteristic features of LRDs. Furthermore, a thorough sampling of the rest-frame UV around ∼1450 Å is essential to accurately derive $M_{UV}$, and the 5100 Å rest-frame optical continuum is needed for determining the bolometric luminosity—$L_{bol}$. With the exception of CEERS, all of our fields benefit from full NIRCam filter coverage, spanning from F090W to F444W, which will cover the rest-frame UV at $z \gtrsim 4$. On the other hand, CEERS has extremely deep (∼29.6 mag at 5$\sigma$) HST/Advanced Camera for Surveys F814W coverage instead, which will also allow us to adequately compute $M_{UV}$ at 1450 Å in the same redshift range. We thus limit our exploration only to objects that have $z > 4$. To do that, we take into account the $p(z)$ and ensure that the 16th percentile, rather than just the median of the $p(z)$, lies above our redshift threshold (e.g., see Valentino et al. 2023). This final selection leaves us with a total of 260 red dots. In Figure 1 we present an overview of our sample selection as well as example SED fits.

### 3.7. Physical Parameters

The physical sizes of the objects in our final sample are extremely compact, with a median effective radius of $r_{eff} < 130$ pc (95% upper limit). This is much smaller when compared to the typical rest-optical sizes of star-forming galaxies measured at $z > 5$ (e.g., see Kartaltepe et al. 2023; Ormerod et al. 2024), but is similar to the extremely compact red objects presented in Labbé et al. (2023a, 2023b) and Baggen et al. (2023) and the LRDs spectroscopically confirmed as BL AGN (Kokorev et al. 2023a; Furtak et al. 2024). Curiously, the dusty galaxies at $z > 7$ explored in Akins et al. (2023) also show the lack of an extended bright component ($r_{eff} < 200$ pc), similar to LRDs. Although not as faint or centrally concentrated as our objects or other LRDs at these redshifts, some of these similarities might imply that these dusty objects can act as potential AGN hosts.

Using the standard relations with the scatter presented in Greene & Ho (2005), and taking into account our best-fit $A_V$ (∼0.6–3.7 mags), we derive the $L_{bol}$ from the 5100 Å continuum, measured directly from the best-fit SEDs. While this is not ideal, and assumes that the red continuum is AGN-dominated, the SED model-dependent values represent our best guess for the intrinsic AGN luminosities. The inferred bolometric luminosities for the compact red objects from our sample thus range from $L_{bol} \simeq 10^{43.5}$ to $10^{46.5}$ erg s$^{-1}$. This range is slightly brighter than that derived in Labbé et al. (2023a), as we are not including any lensed fields, and is thus likely to fail to detect intrinsically fainter LRDs. We show the dust-corrected and observed $L_{bol}$ values in Figure 2.

In Figure 3, we explore how the observed $M_{UV}$ values of our LRDs compare to the expectations derived from the dust-corrected bolometric luminosity (Shen et al. 2020). Given our median $\langle A_V \rangle \sim 1.6$, we expect the UV extinction to be large, with $A_{UV} \sim 9$, but what we find is $\langle A_{UV} \rangle \sim 2.5$ (similar to, e.g., Greene et al. 2024; Maiolino et al. 2024; Matthee et al. 2024), a difference of more than 6 magnitudes. Adding to this, the shape of the rest-UV spectrum, while faint, does not hint at any dust extinction. This suggests that a second component, different from a reddened AGN spectrum, is present in LRDs, although with our current data its origin cannot be determined.

The final table—which contains photometry, sizes, and the physical parameters we derive for our sample—is available in full online.[11] We show an excerpt of the full table in the Appendix.

## 4. The Number Density of Compact Red Sources

### 4.1. Estimating Effective Volumes

One of the key motivations for our work is to conduct an unbiased search for LRDs in some of the deepest blank fields observed with JWST. Our goal is to extend the existing luminosity functions that have been deduced from spectroscopic samples to a larger sample covering a wider area. By applying the color and size criteria that have been adopted in recent LRD studies, such as those discussed in Greene et al. (2024) and Labbé et al. (2023a), we aim to exploit the large areas in our blank fields to get better statistics, particularly at the bright and faint ends. This approach should allow us to examine how much these objects contribute to the observed $L_{bol}$ and $M_{UV}$ number densities. However, as we are working with a photometrically selected sample, our analysis will be focused on the aggregate characteristics of the LRDs, rather than on detailed examinations of individual objects.

Focusing only on the blank fields allows us to estimate the effective volumes for our objects in a rather simple way. In order to measure the observed number densities of our sample, we follow the standard $V_{max}$ method (Schmidt 1968). The $1/V_{max}$ estimator has the advantage of simplicity and does not require prior assumptions on the functional form for the luminosity distribution, which is ideal for LRDs, since their intrinsic luminosity/mass distributions are unknown. To compute the number density for some property—$x$—we can then say

$$\Phi(x) = \frac{1}{\Delta x} \sum_i V_{max,i}(A, z_{min}, z_{max})^{-1},$$

where $\Delta x$ is the width of the bin and $V_{max,i}$ is the maximum volume over which a source can be detected. In return, $V_{max,i}$ depends on the effective survey area ($A$), the lower redshift bin boundary ($z_{min}$ ), and the maximum observable redshift ($z_{max}$). The latter is computed empirically from the detection limits of the survey, given the selection criteria, and cannot exceed the maximum redshift of the bin.

[11] https://github.com/VasilyKokorev/lrd_phot

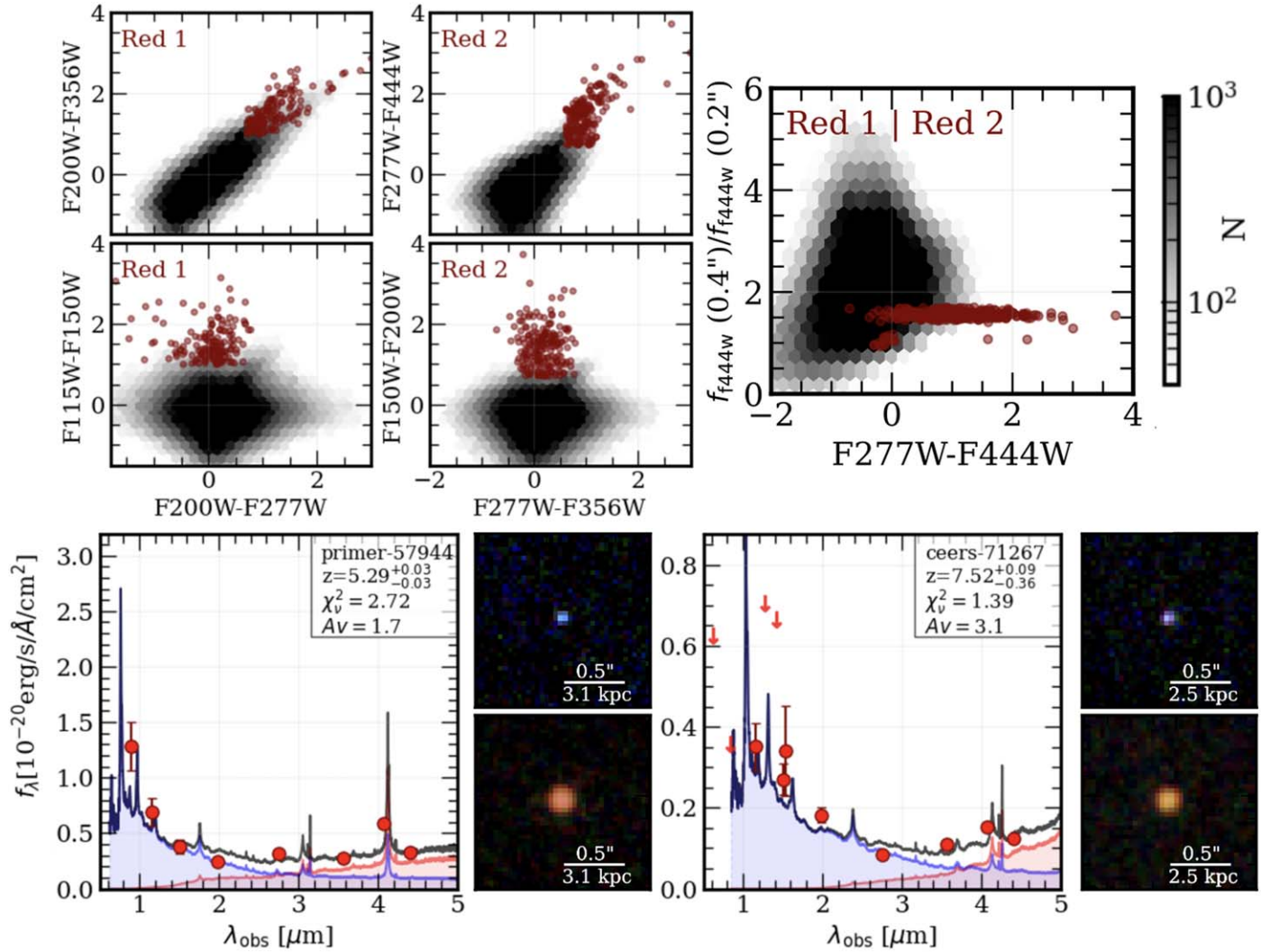


**Figure 1.** Selection and analysis of LRD candidates. Top: sample selection criteria. The left and central panels show modified "red 1" ($z \lesssim 6$) and "red 2" ($z \gtrsim 6$) color–color cuts from Labbé et al. (2023a). The right panel shows the compactness cut of our sample. The selected objects are highlighted as maroon circles, while the grayscale hexbins show the full catalog. The compact red sources are clear outliers in the color–color-compactness space. The color bar is shared between all plots. Bottom: an example of best-fit SEDs to the photometry of LRD candidates with the dust-free (blue) and dusty (red) AGN templates (Vanden Berk et al. 2001; Glikman et al. 2006) at representative redshifts of $z \sim 6$ and $z \sim 8$. The combined model is shown in black. Detections ($>3\sigma$) are shown as red circles, while upper limits (primarily from HST) are shown as downward arrows. On the right of each SED, we show 1.″5 color composite cutouts in the short (F115W/F150W/F200W) and long (F277W/F356W/F444W) NIRCam filters.

We obtain the total survey areas by adding up all the nonmasked pixels in our detection images, as presented in Table 1. Given how bright we require our objects to be (F444W $<$ 27.7 mags at $S/N > 14$), it might seem that $z_{max}$ would always exceed the maximum redshift of the bin, but this does not take into account the fact that our objects have to be detected in at least four bands (at $>3\sigma$) to make color selection robust. We choose to remain conservative with our volume corrections, by only requiring one band per color combination to be detected. The $z_{max}$ values for each object are then estimated by considering our color selection laid out in Section 3. The uncertainties on our number densities are then derived in the following way. We consider the standard errors arising from Poisson statistics and compute them as prescribed in Gehrels (1986). Given that we only consider a photometric sample in our work, the uncertainty on the photometric redshift has to be taken into account appropriately in order to derive realistic errors on the physical parameters and number densities. To do that, we follow the approach described in Marchesini et al. (2009). Briefly, for each object, we use Monte Carlo simulations to determine whether the objects fall into the redshift bin by considering their $p(z)$. The final uncertainties are then a quadrature sum of the Poisson and $p(z)$ errors.

Accounting for magnitude incompleteness effects as it is normally done for galaxy luminosity functions is not possible in our case, since it relies on making assumptions regarding the intrinsic source distributions. However, as Labbé et al. (2023a) already note, the requirement for objects to be bright in the detection band should lessen, but not eliminate altogether, the effect of magnitude incompleteness. Given that our sources are compact, we also expect that all of them will be detected above the brightness limit, diminishing the need to consider the incompleteness as a function of surface brightness. Despite the complex selection function, it is still possible to define a limit beyond which the derived number densities, for the observed quantities, are expected to become incomplete. We will discuss this in the next sections.

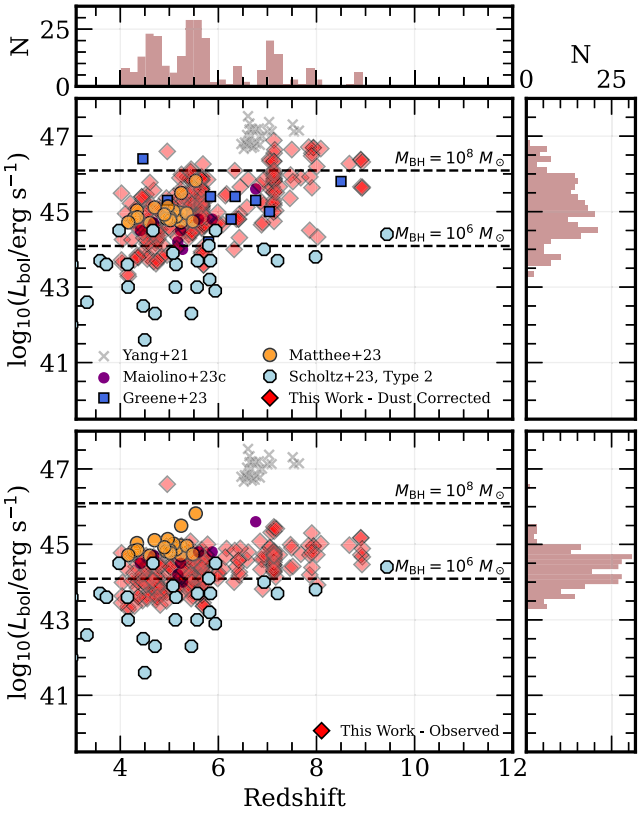


**Figure 2.** Top: distribution of $L_{bol}$ assuming an AGN-dominated rest-frame optical continuum, with best-fit dust correction applied. Our compact sources span a wide range of luminosities across the redshift range of interest. We contrast our results with BL AGN from Greene et al. (2024; blue squares) and Matthee et al. (2024; orange circles), $z > 6.5$ quasars from Yang et al. (2021; gray crosses), high-$z$ AGN from Maiolino et al. (2024; magenta circles), and finally objects hosting Type 2 AGN from Scholtz et al. (2023; light blue circles). Assuming $\lambda_{edd} = 1$, we show what $L_{bol}$ would correspond to $M_{BH} = 10^{6-8} M_\odot$ (dashed lines). Bottom: the same as before, but we show the distribution of $L_{bol}$ without correcting for the best-fit dust attenuation. Our final sample has a median $A_V \sim 1.6^{+1.1}_{-1.0}$. On the side of each panel, we also show histograms highlighting the redshift and $L_{bol}$ distributions.

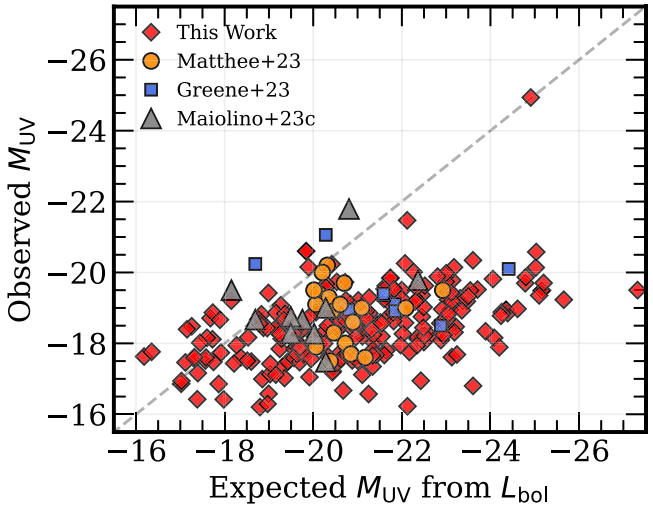


**Figure 3.** Observed $M_{UV}$ compared to the $M_{UV}$ expected from the dust-corrected $L_{bol}$. We derive the expected $M_{UV}$ values by following the relation from Shen et al. (2020). We also show the data for red dots from Greene et al. (2024; blue squares) and Matthee et al. (2024; orange circles), as well as BL AGN at $z > 4$ from Maiolino et al. (2024; gray triangles). The gray dotted line shows the 1:1 relation. The observed $M_{UV}$ we derive is fainter than the expected value, with $A_{UV}$ varying from ∼0.6 to 4.2. While extreme, the UV attenuation is more than 5 magnitudes smaller when compared to the values expected given our best-fit $A_V$.

### 4.2. UVLF

In Figure 4, we present the UVLFs in two redshift bins, at $z \sim 5$ and $z \sim 7$, derived from the continuum luminosity at rest frame 1450 Å, as normally done for blue quasars. We list the number counts alongside the uncertainties in Table 2. The widths of our redshift bins were chosen to best align with the current literature results, for ease of comparison, as well as to ensure that the photometric redshift uncertainties have a minimal impact on the luminosity functions.

At $z \sim 5$, we find that the number densities of our red-color-selected AGN are ∼2 dex higher compared to the UV-selected quasars at similar magnitudes, depending on the extrapolation (Niida et al. 2020). As an upper limit on the number density of quasars at $z \sim 5$, we also compare to the results presented in Kulkarni et al. (2019), which combine both UV-bright quasars ($M_{UV} < -24$) and UV-faint X-ray-detected AGN (Giallongo et al. 2019) in their UVLFs.

Before comparing to current observational results (Kocevski et al. 2023; Greene et al. 2024; Matthee et al. 2024), we note that it is difficult to accurately define the selection function for spectroscopically observed samples and therefore derive the $V_{max}$ corrections. As such, the number densities computed in these works should be treated as lower limits. In our case, the sample is selected via photometry and we derive our $V_{max}$ correction based on the selection criteria alone. This is done to avoid significantly overestimating the number counts, thus misrepresenting the true abundance of the red dots. It is also unlikely that this difference is a result of brown dwarfs contaminating our sample here, since we introduce an additional color cut from Greene et al. (2024), based on the spectra from Burgasser et al. (2024).

Taking the uncertainties into account, we find that our UV number counts are consistent with JWST-selected red BL AGN samples (Labbé et al. 2023a; Greene et al. 2024; Matthee et al. 2024), at least at $M_{UV} \sim -19$ and brighter. Confirming the initial findings for the UNCOVER red dots presented in Greene et al. (2024) and Labbé et al. (2023a), we also find that our sample accounts for ∼10%–30% of the total BL AGN populations at high-$z$ (Harikane et al. 2023; Maiolino et al. 2024) and is largely comparable to the X-ray-selected quasars from Giallongo et al. (2019), although in the case of the latter we infer higher number densities at fainter UV magnitudes. However, it is worth noting that differences between the resolution of Chandra X-ray data and optical light from HST can lead to uncertainties when associating X-ray emission to the galaxies being present in the same patch of the sky. Curiously enough, the recovered scarcity of compact red sources compared to galaxies is in stark contrast to the density of Type 2 AGN hosts inferred from the recent JADES spectra (Scholtz et al. 2023), which report as much as a 20% contribution to the galaxy luminosity functions at $z \sim 5$.

When moving to the $z \sim 7$ bin, the results for the UVLF at both bright and faint luminosities are inconclusive, due to the limited number of objects and the uncertainty on the photometric redshifts. However, we are again consistent with the number densities of the UNCOVER BL AGN from Greene et al. (2024). Comparing to the luminosity functions of

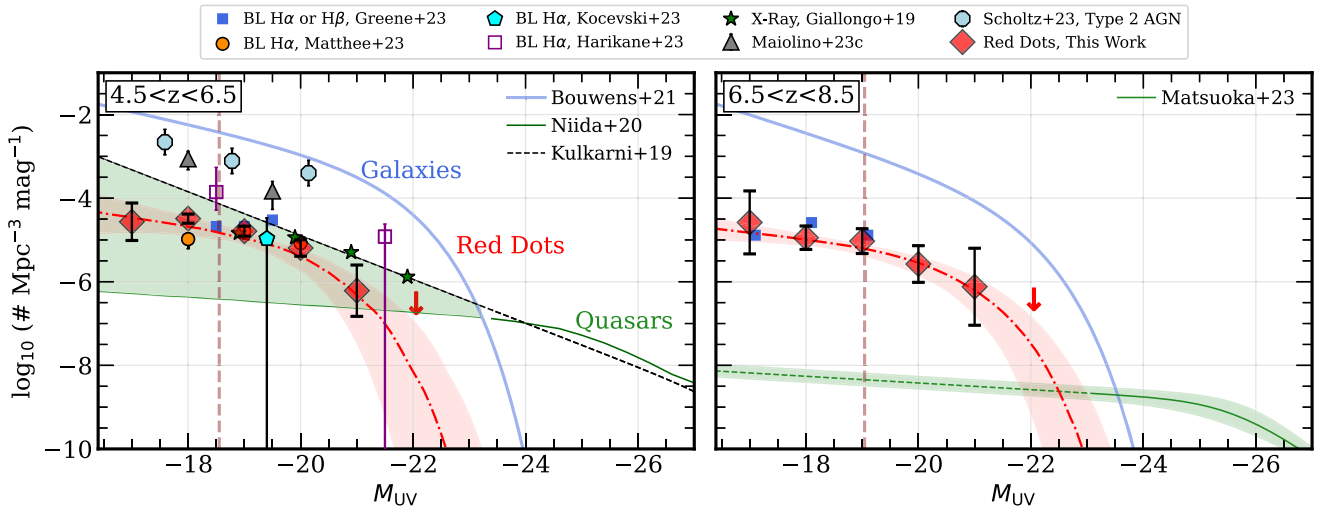


**Figure 4.** The UVLF for the LRDs in our sample in the $z \in [4.5, 6.5]$ (left) and $z \in [6.5, 8.5]$ (right) bins (blue), derived from the observed rest-UV light. The upper limits are shown by downward-pointing arrows. The dashed red line and the shaded area correspond to our best-fit Schechter function and its 68% confidence interval, respectively. The vertical maroon lines highlight the $M_{\rm UV}$ completeness limit calculated from the average depth of the F814W/F090W bands. We compare our derived number densities to the luminosity functions of the Lyman-break galaxies from Bouwens et al. (2021; solid blue line), the extrapolated quasar UVLF relations from Niida et al. (2020) at $z \sim 5$, as well as an upper bound provided by Kulkarni et al. (2019; green lines). At $z \sim 7$, in green, we show the UVLF derived from bright quasars from Matsuoka et al. (2023). We highlight the spectroscopically identified LRDs from Greene et al. (2024; blue squares), Matthee et al. (2024; orange circles) and Kocevski et al. (2023; blue pentagon). Furthermore, we show the densities of BL AGN quasars from Maiolino et al. (2024; gray triangles) and Harikane et al. (2023; open squares). The green stars show the UV number densities of the X-ray-detected quasars at $z \sim 5$ from Giallongo et al. (2019). Finally, the light blue octagons represent the UVLFs derived for galaxies hosting Type 2 AGN from Scholtz et al. (2023). We offset some of the literature points by $\pm 0.05$ dex horizontally for visualization purposes. Note that our measured UV luminosities do not decompose the AGN emission from the potential galaxy light.

UV-selected quasars from Matsuoka et al. (2023) at $z \sim 7$, and extrapolating to fainter magnitudes, we find a 2−3 dex offset between the number densities at $M_{\rm UV} > -22$, roughly a factor of 10 larger than in the lower redshift bin. Alongside our UVLF, we also highlight the median $M_{\rm UV}$ $5\sigma$ completeness limits. These are derived by considering the depths of the filters covering the rest frame ∼1450 Å at a given redshift, and whether a source of a given $M_{\rm UV}$ would be detected at signal-to-noise ratio $> 5$. As such, we should be complete down to $M_{\rm UV} \sim -18.5$ at $z = 5$ and $M_{\rm UV} \sim -19.0$ at $z = 7$.

Following Bouwens et al. (2015), we fit our observed UV number densities with a Schechter (1976) function, allowing all parameters to be free. We only fit data brighter than $M_{\rm UV} = -18.5$ at $z \simeq 5$ and $M_{\rm UV} = -19.0$ at $z \simeq 7$, as our number densities indicate that we are likely becoming incomplete at such faint magnitudes. The best fit is shown in Figure 4 and the parameters are listed in Table 3. In both redshift bins, we find that our red compact objects constitute roughly 3%–5% of the total star-forming galaxy populations (Bouwens et al. 2021), consistent with the spectroscopic samples of red dots (Greene et al. 2024). We also report shallower faint-end slopes compared to star-forming galaxies, although it is likely that the observed flattening of the UVLF for LRDs is induced by the incompleteness of our sample at fainter UV magnitudes, rather than any lack of compact red sources at fainter UV magnitudes. Deeper surveys would be required to robustly constrain the faint-end slope of the LRDs. It appears that the LRD luminosities start to become comparable to or even outshine galaxies at brighter ($M_{\rm UV} \sim -23$) magnitudes, which is particularly prominent in the $z \sim 7$ bin. This might be an expected consequence of the assembly of increasingly massive BHs with cosmic time (e.g., see Piana et al. 2022) or selection effects (see Volonteri et al. 2017), but we note that our number counts for the brightest objects are uncertain due to the limited amount of detections available.

Provided that our color and morphology selection is comparably successful at identifying reddened AGN as previously shown (Labbé et al. 2023a; Greene et al. 2024), it appears that the compact red sources identified in blank JWST fields are ∼1–2 dex more numerous compared to the pre-JWST studies of known UV-selected faint quasars ($M_{\rm UV} > -21$). While this trend has been consistently reemerging in the new JWST results (e.g., Kokorev et al. 2023a; Pacucci et al. 2023; Furtak et al. 2024; Maiolino et al. 2024), it is worth noting that earlier works have already hinted that the number density of UV-faint, dusty, active BHs could have been much higher than previously thought (Laporte et al. 2017; Morishita et al. 2020; Fujimoto et al. 2022). For example, both Fujimoto et al. (2022) and Morishita et al. (2020) find that the less luminous red quasar population could be anywhere from 10 to 100 times more common at $z \sim 7$–8, compared to quasar luminosity functions at $z \sim 6$, constructed from ground-based data sets (e.g., Matsuoka et al. 2018; Kato et al. 2020; Niida et al. 2020). The results of this work, together with the recent efforts to study compact red sources, therefore imply that these faint quasar populations, missed by previous surveys, are now being uncovered by the deep and rich multiwavelength photometry and spectra from JWST. It is also important to highlight that if we extrapolate our UVLF to brighter magnitudes, the number density of LRDs becomes comparable to and then drops below the density of UV-selected quasars. Currently, however, it is not possible to speculate whether this is a real physical effect or simply a consequence of insufficient volumes sampled.

### 4.3. Bolometric Luminosity Function

Our SED fitting results show that the fraction of the UV light contributing to the total luminosity is small, as a result of

**Table 2**
Bolometric and UV ($\lambda_{rest} = 1450$ Å) LFs, as Well as an SMBH Mass Function, for Our Sample of LRDs

| UV Luminosity | | |
|---|---|---|
| $M_{UV}$ [ABmag] | $N$ | $\Phi$/[cMpc$^{-3}$ mag$^{-1}$] |
| $4.5 < z < 6.5$ | | |
| −17.0 | 19 | $-4.56 \pm 0.45$ |
| −18.0 | 68 | $-4.49 \pm 0.11$ |
| −19.0 | 53 | $-4.79 \pm 0.12$ |
| −20.0 | 21 | $-5.19 \pm 0.20$ |
| −21.0 | 2 | $-6.21 \pm 0.61$ |
| −22.0 | 1 | $< -6.52$ |
| $6.5 < z < 8.5$ | | |
| -17.0 | 5 | $-4.58 \pm 0.75$ |
| -18.0 | 23 | $-4.95 \pm 0.28$ |
| -19.0 | 29 | $-5.02 \pm 0.30$ |
| -20.0 | 9 | $-5.58 \pm 0.44$ |
| -21.0 | 2 | $-6.12 \pm 0.92$ |
| -22.0 | 1 | $< -6.42$ |
| Bolometric Luminosity | | |
| $\log_{10}(L_{bol}/\mathrm{erg\ s^{-1}})$ | $N$ | $\Phi$ / [cMpc$^{-3}$ dex$^{-1}$] |
| $4.5 < z < 6.5$ | | |
| 44.0 | 46 | $-4.37 \pm 0.20$ |
| 45.0 | 93 | $-4.48 \pm 0.10$ |
| 46.0 | 26 | $-5.10 \pm 0.18$ |
| 47.0 | 1 | <–5.62 |
| $6.5 < z < 8.5$ | | |
| 44.0 | 1 | >–5.48 |
| 45.0 | 14 | $-4.51 \pm 0.23$ |
| 46.0 | 33 | $-4.76 \pm 0.15$ |
| 47.0 | 9 | $-5.47 \pm 0.29$ |
| BH Mass ($\lambda_{edd} = 1$) | | |
| $\log_{10}(M_{BH}/M_{\odot})$ | $N$ | $\Phi$ / [cMpc$^{-3}$ dex$^{-1}$] |
| $4.5 < z < 6.5$ | | |
| 6.0 | 39 | $-4.19 \pm 0.39$ |
| 6.5 | 44 | $-4.40 \pm 0.24$ |
| 7.0 | 40 | $-4.60 \pm 0.24$ |
| 7.5 | 21 | $-4.89 \pm 0.10$ |
| 8.0 | 2 | $-5.91 \pm 0.33$ |
| 8.5 | 1 | $-6.21 \pm 0.45$ |

**Table 3**
Best-fit Schechter Parameters for the Rest-frame UVLF at $\lambda_{rest} = 1450$ Å, across Blank JWST Fields

| $\langle z \rangle$ | $M^*_{1450}$ (ABmag) | $\phi^*$ ($10^{-3}$ Mpc$^{-3}$) | $\alpha$ |
|---|---|---|---|
| 5 | $-20.64 \pm 0.67$ | $0.008 \pm 0.003$ | $-1.76 \pm 0.67$ |
| 7 | $-20.67 \pm 0.76$ | $0.005 \pm 0.002$ | $-1.46 \pm 0.37$ |

significant dust reddening ($A_V = 0.6$–$2.7$) in these objects. Even with spectra in hand (e.g., Greene et al. 2024), it is not easy to establish the origins of the rest-UV light, which could be AGN light, either scattered or transmitted through patchy dust clouds, or unobscured light from star formation in the host galaxy. As such, while we put our LRDs in the context of their observed UV luminosities, this does not explicitly describe the physics of the potential AGN these compact objects host. Due to that, and also to carry out a comparison with existing spectroscopic bolometric luminosity functions of dusty BL AGN, we also present bolometric luminosity functions in Figure 5 and Table 2. While dust attenuation, estimated from SED fitting, can be an important source of uncertainty, we note that even if all our $A_V$ values were grossly overestimated, this would only change the dust-corrected $L_{bol}$ by a factor of $\times 5$, given the average $A_V \sim 1.6$. This would thus only impact the number densities by $\sim \sqrt{5}$ on average, which is insignificant when compared to the Poisson and $z_{phot}$ errors. Finally, to account for the potential presence of emission lines with high EW, we incorporate the additional $\sim$0.1 systematic shift in $A_V$ and apply it to the uncertainties on the $L_{bol}$.

Understanding where the bolometric luminosity functions start to become incomplete is less straightforward compared to the observed quantities like $M_{UV}$, as the former also rely on dust correction derived via SED modeling and the assumptions made regarding the AGN contribution to the rest-frame optical emission. For this reason, we do not define a completeness cut, like we do for $M_{UV}$, but for each bin of bolometric luminosity with a width of 1 dex, we also compute the $V_{max}$ correction, as described in Section 4.1.

Our number densities again confirm that the red compact AGN candidates are roughly 100 times more abundant compared to the UV-selected AGN at similar intrinsic luminosities (Shen et al. 2020) at $z \sim 5$. The $L_{bol}$ number densities that we recover are comparable to the previous results for these objects derived in Greene et al. (2024), Labbé et al. (2023a), and Matthee et al. (2024) for $L_{bol} - 10^{45-46}$ erg s$^{-1}$. Curiously, however, we find a factor of 10 more LRDs compared to Greene et al. (2024) at $L_{bol} \sim 10^{44}$ erg s$^{-1}$. Nominally, the median NIRSpec depth at 4 $\mu$m of the UNCOVER follow-up of A2744 is shallower compared to the fields we examine; as such, it is perhaps unsurprising that we can recover a large fraction of intrinsically faint objects. However, since the $L_{bol}$ is not an observed quantity and depends on SED modeling to calculate the dust correction, it is difficult to ascertain whether the higher number densities we recover are indeed caused by the depth difference or simply the bias caused by the spectroscopic-only sample selection and lensed volumes in UNCOVER. Moreover, the mask design of the UNCOVER NIRSpec observations in the A2744 field was also driven by optimizing the MSA coverage to include other targets of interest and was not just limited to LRDs. This, in return, induces selection effects that would not be possible to trace back and correct for.

We additionally compare our bolometric luminosity function to the latest version of the semi-analytic DELPHI models (Dayal et al. 2019, 2024). In brief, these models follow the seeding and growth of BHs from $z \sim 40$ down to $z \sim 4.5$. Included are also all the key processes of the merger- and accretion-driven assembly of dark matter halos and their baryonic components (including BHs). The model also follows star formation and BH growth and their respective feedbacks in determining the assembly of these early systems. Finally, DELPHI models also include key dust processes to yield dust-to-stellar mass ratios, with a baseline constructed against the latest ALMA observations (Dayal et al. 2022; Mauerhofer & Dayal 2023). All of this was specifically done to ensure DELPHI can reproduce both the

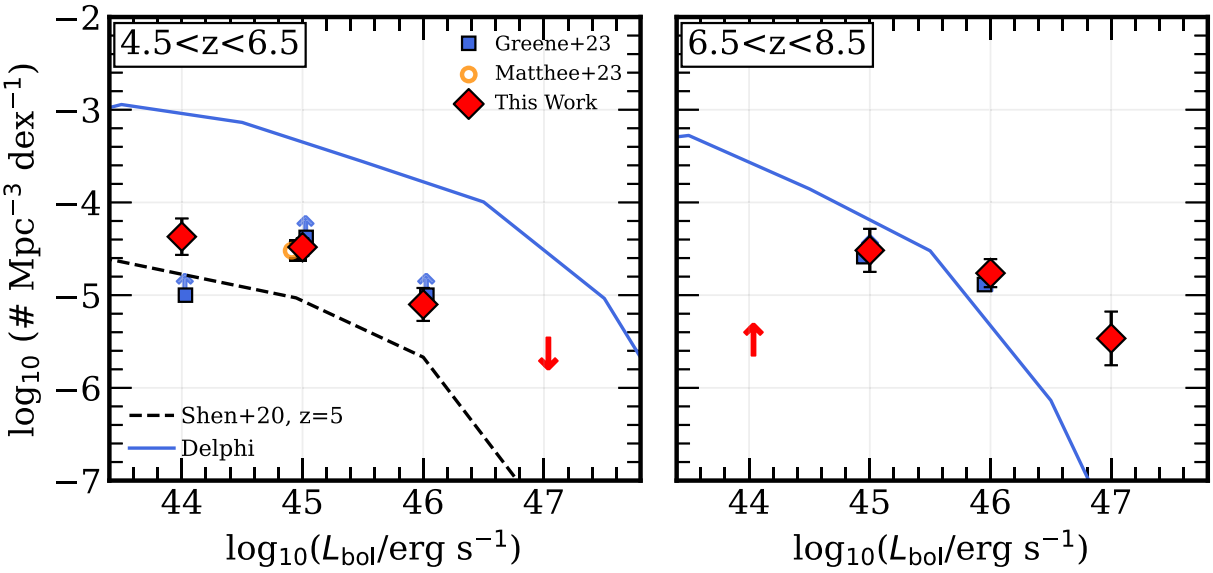


**Figure 5.** Bolometric luminosity functions in the $z \in [4.5, 6.5]$ (left) and $z \in [6.5, 8.5]$ (right) bins, derived from $L_{5100}$, assuming the rest-frame optical continuum is AGN-dominated. The number densities have been $V_{max}$- and completeness-corrected. The uncertainties are derived from Poisson noise (Gehrels 1986). The arrows show the upper limits on the derived number densities. The blue squares show the upper limits derived for spectroscopically confirmed LRDs in the UNCOVER data from Greene et al. (2024). In addition, in the lowest-redshift bin, we show the NIRCam grism result of Matthee et al. (2024; open circle). The dashed lines show the pre-JWST $L_{bol}$ relation derived in Shen et al. (2020). Finally, the blue lines show the luminosity function from the Delphi semi-analytic models (Dayal et al. 2019) that grow SMBHs from seeds.

intrinsically faint and reddened sources in the recent literature, i.e., the LRDs.

We find that while our observations are comparable to DELPHI results at $L_{bol} < 10^{47}$ erg s$^{-1}$ at $z \sim 7$, these models fail to reproduce the high number density of bright objects we report. At $z \sim 5$, on the other hand, our densities consistently fall 1 dex below DELPHI predictions. This, in return, could suggest that the fraction of dusty AGN is diminishing toward later times, as they potentially transition to unobscured quasars (Fu et al. 2017; Fujimoto et al. 2022).

Finally, we also see a higher prevalence of intrinsically brighter objects at $\sim L_{bol} - 10^{47}$, which is a likely consequence of the larger volumes sampled in our analysis. As already mentioned in Greene et al. (2024), however, it is worth noting that the uncertainties on the $L_{bol}$–$L_{5100}$ relation, dust correction, and assuming that these objects are dominated by AGN light at the rest-frame optical could cause objects to scatter upward into the high-luminosity bins. We only recover a single object above $L_{bol} = 10^{47}$ erg s$^{-1}$ at $z \sim 5$ and below $L_{bol} = 10^{44}$ erg s$^{-1}$ at $z \sim 7$, respectively. As this is insufficient to properly compute the luminosity functions, these are shown as upper (lower) limits in Figure 5, derived by combining the Poisson (Gehrels 1986) and photo-$z$ (Marchesini et al. 2009) uncertainties.

### 4.4. The z ∼ 5 SMBH Mass Function

With the data we have obtained, we will now derive and describe the measurement for the SMBH mass function that our compact objects potentially host. Computing the mass of the central BH generally requires knowledge of the width of the broad lines (e.g., H$\alpha$, H$\beta$ in rest-optical, or Mg II in rest-UV), coupled with the luminosity of their broad components or the luminosity derived from the AGN continuum at $\lambda_{rest} = 5100$ Å (see, e.g., Kaspi et al. 2000; Greene & Ho 2005).

While the secure determination of the BH mass in our compact objects is not possible, due to the photometric nature of the sample, we can still place a lower limit on the BH masses ($M_{BH}$) by making a set of conservative assumptions. To do that, we adopt a scenario where all our AGN candidates accrete at the Eddington rate (the physical limit at which outward radiation pressure balances inward gravitational force), such that $L_{bol} \sim L_{edd}$, where $L_{edd}$ is directly proportional to $M_{BH}$. While in the literature, the Eddington rate ($\lambda_{edd}$) for confirmed AGN in LRDs was found to vary between 10% and 40% (Kokorev et al. 2023a; Furtak et al. 2024; Greene et al. 2024), we would like to remain conservative and compute a lower limit on the $M_{BH}$. It is also worth noting that, given this range of $\lambda_{edd}$ in the literature, this is still small compared to other sources of uncertainty in our work.

We calculate the $M_{BH}$ directly from the dust-corrected $L_{bol}$ and compute the SMBH mass function as described in the previous sections. We present our SMBH mass function in Figure 6 and Table 2, binned into 0.5 dex intervals to allow a direct comparison with the existing observational and theoretical results in this redshift range. We limit this investigation to the $z \sim 5$ range only. As before, we note that the effect of the $A_V$ uncertainty on our number densities is expected to be at most $\sim\sqrt{5}$, largely overshadowed by the Poisson and redshift errors.

We are now in a position to compare our mass function to the existing samples of both bright and faint quasars at $z \sim 5$. We start with the latest ground-based examination of the quasar mass function at $z \sim 4$ from He et al. (2024). The authors focus on a sample of ∼1500 faint BL AGN, from a combined Hyper Suprime-Cam (HSC) and SDSS data set, allowing them to extend their examination to a low-mass range we are most interested in ($M_{BH} \simeq 10^{7-8}\ M_\odot$). We find that while our result is consistent with the ground-based mass function in the high-mass regime $M_{BH} > 10^8\ M_\odot$, our number densities diverge below that mass and continue to rise up to $\sim 10^{-4}$ cMpc$^{-3}$ at $M_{BH} \simeq 10^6\ M_\odot$. Barring the color selection, it is possible that

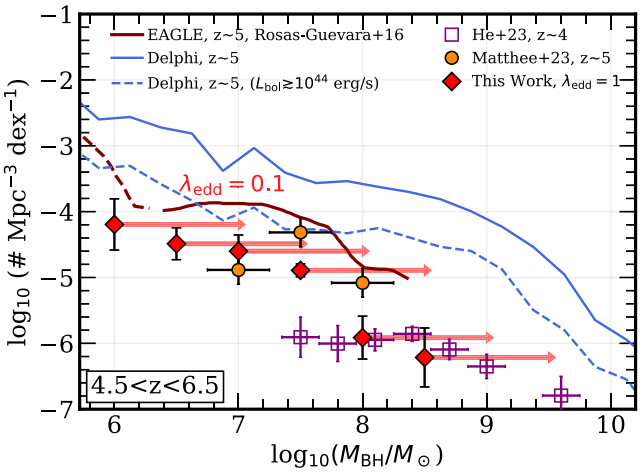


**Figure 6.** The SMBH mass function, assuming $\lambda_{edd} = 1$, of our sample in the $4.5 < z < 6.5$ range. The red arrows show how our mass function would change if we assumed a lower Eddington ratio of 10%. We overlay the SMBH mass function from Matthee et al. (2024) at $z \sim 5$ in orange and the HSC +SDSS-derived BH mass function from He et al. (2024) in magenta. The maroon line shows the results from the EAGLE simulation at $z \sim 5$ (Rosas-Guevara et al. 2016). The solid and dashed blue lines show the results from the Delphi (Dayal et al. 2014, 2019, 2020) simulations for all and bright ($L_{bol} \gtrsim 10^{44}$ erg s$^{-1}$) BH, respectively. The measured number densities of our LRDs agree well with the spectroscopic sample from Matthee et al. (2024) and the simulations, given $\lambda_{edd} \sim 1$.

this effect is purely observational, as the SDSS/HSC detection limits in the rest-UV are much shallower compared to the JWST fields we explore.

Furthermore, we contrast our result to the BH mass function at $z \sim 5$ based on a sample of LRDs from the slitless JWST data, presented in Matthee et al. (2024). Given the uncertainties, we find our results to be consistent within $1\sigma$, although we do not find a sharp drop-off in the number densities at $M_{BH} < 10^7\ M_\odot$, likely driven by the low-mass incompleteness of the grism data as mentioned in Matthee et al. (2024).

Naturally, the fact that both our result and Matthee et al. (2024) find more low-mass BHs compared to He et al. (2024) is unsurprising, given the depth and wavelength coverage of the JWST data. Quite curiously, however, it appears that the mass function derived from dusty compact LRDs seems to nicely continue the rising trend of ground-based data and extend the SMBH mass functions toward $M_{BH} \sim 10^6\ M_\odot$. In this redshift range, the maximum volume sampled by our multifield investigation is roughly equal to $\sim 3.0 \times 10^6$ cMpc$^3$. Therefore, taking into account the results of He et al. (2024), we should expect only one object with $M_{BH} \sim 10^{8.5}\ M_\odot$ in our images, which indeed is the case. The detection of AGN hosting BHs with masses larger than that would, however, require survey sizes 10 to 20 times larger.

Before drawing conclusions, we would like to conduct a final check and compare our result to the hydrodynamical simulation EAGLE (Rosas-Guevara et al. 2016) and the semi-analytic Delphi (Dayal et al. 2014, 2019, 2020, 2024) simulations describing the masses of SMBHs in the same redshift range. We limit our examination of the Delphi models to the bright ($L_{bol} \gtrsim 10^{44}$ erg s$^{-1}$) regime to match the same luminosity range covered by our objects. In the intermediate- to low-mass end ($M_{BH} < 10^{7.5}\ M_\odot$), our results are in broad ($\sim 2\sigma$) agreement with both EAGLE and Delphi, although in both cases we start to see a significant difference in the number densities as we move to higher masses. Perhaps a worthwhile question to ask in this case is whether more of these high-mass BHs would be found in larger areas. We will discuss this in a later section.

Examining both the UV and bolometric luminosity functions, we note that LRDs only represent ~25% of the total Type I (BL) AGN population, as inferred by Harikane et al. (2023) and Maiolino et al. (2024), even less so compared to the most recent examination of Type II AGN hosts from JADES (Scholtz et al. 2023), where LRDs are 30–40 times less numerous. Taking this into account, we can conclude that, at least at $z \sim 5$, LRDs appear to represent at most 1% of the total accreting BH population over the $L_{bol} \sim 10^{44-47}$ erg s$^{-1}$ range. The fact that LRDs are truly a distinct population of dusty BL AGN can therefore explain the observed ~2 dex disparity between our results and simulations. Finally, we would like to reiterate that our investigation of the BH mass function relies on assuming the most conservative case of accretion at exactly the Eddington rate, as we do not want to erroneously overestimate the number of high-mass BHs. Keeping that in mind, in Figure 6 we also show how our mass functions would change if we were to assume an Eddington ratio of 10% instead. In this case, we find that while our number densities compared to UV samples are still high, we now more closely match the abundance of high-mass SMBHs predicted by DELPHI. However, until broad emission-line observations for all our sources are available, the value of $\lambda_{edd}$ will remain uncertain.

## 5. Discussion and Summary

### 5.1. Abundance of Bright Compact Sources

Previously limited to UV-selected samples at $z \lesssim 6$ (Kashikawa et al. 2015; Bañados et al. 2018; Matsuoka et al. 2018; Inayoshi et al. 2020; Wang et al. 2021; Fan et al. 2023), we are now able to use JWST to reveal the presence of AGN during (e.g., Kocevski et al. 2023; Übler et al. 2023; Matthee et al. 2024) and even beyond the epoch of reionization (e.g., Furtak et al. 2023b; Goulding et al. 2023; Kokorev et al. 2023a; Larson et al. 2023; Maiolino et al. 2023; Bogdan et al. 2024; Lambrides et al. 2024) only hundreds of millions of years after the big bang. Standing out among these early studies of active BHs is the population of reddened Type I AGN, the so called LRDs (Greene et al. 2024; Labbé et al. 2023a; Matthee et al. 2024).

While the study of this unique population has been mostly limited to small spectroscopic samples, most recent efforts focused on the expansive A2744 JWST data set (Labbé et al. 2023a) have shown great promise at using a combination of NIRCam colors and morphology to identify reddened AGN. This initial photometric selection was shown to be remarkably successful, with ~80% of targets indeed confirmed as $z > 5$ dusty BL AGN (Fujimoto et al. 2023c; Furtak et al. 2023b; Kokorev et al. 2023a; Greene et al. 2024). It is clear that these objects play an important role in the story of BH growth at early times, although so far a systematic review of these enigmatic AGN across multiple fields has not been undertaken.

Motivated by the success of this photometric selection, we present a sample of 260 reddened BL AGN candidates in the $4 < z < 9$ redshift range, covering four separate blank JWST

fields with a total area of ∼640 arcmin$^2$. We uniformly reduce the NIRCam JWST data from a variety of public programs, complementing our photometric coverage with archival HST observations. We perform a color and morphology selection to identify the most promising compact objects that display a dichotomy in their observed SED shapes, namely a blue rest-UV continuum and a red power-law-like rest-optical. Our sample is publicly available, and we present a full description of our catalog in Table 4.

Using model fitting, we derive photometric redshifts as well as a range of physical parameters, including $A_V$, $M_{UV}$, and dust-corrected $L_{bol}$. We split our objects into two redshifts bins at $z \sim 5$ and $z \sim 7$ and explore their contribution to the UV and bolometric luminosity functions of star-forming galaxies as well as UV-selected quasars. Consistent with previous works (Greene et al. 2024; Maiolino et al. 2024; Matthee et al. 2024) exploring high-$z$ BL AGN, we find that the number densities of these objects at $z > 5$ are surprisingly high, in excess of $\times 100$ compared to faint UV-selected quasars (e.g., Niida et al. 2020; He et al. 2024), while also accounting for ∼20% of the total BL AGN population (Harikane et al. 2023; Maiolino et al. 2024) and ∼1%–2% of UV-selected star-forming galaxies (e.g., Bouwens et al. 2021). Moreover, while some of these objects were potentially pinned down as potential sources of reionization in their local environment (Fujimoto et al. 2023c), it appears that their UV luminosities are still insufficient to contribute to reionization in a significant way (Dayal et al. 2024).

Assuming accretion at the Eddington rate, we also place a lower limit on the $M_{BH}$ of our objects, finding that some of these can already be very massive ($M_{BH} > 10^7\ M_\odot$) only a few hundred years after the big bang. Using these masses, we were also able to construct our prediction for the SMBH mass function and, for the first time, extend it to the low-mass ($<10^7\ M_\odot$) regime. We find that our mass function results are completely consistent with the number densities derived for faint dusty AGN from Matthee et al. (2024) at intermediate masses and are comparable to those from UV-selected samples at high mass (He et al. 2024). We note, however, that while their number densities are similar, the sample presented in He et al. (2024) consists of unobscured quasars, and not LRDs, which are thought to be dust-obscured AGN. We find that both hydrodynamical and semi-analytic predictions for the number of BHs at this redshift match our observations below $\sim 10^{7.5}\ M_\odot$, although they start to disagree by almost 2 dex at higher masses. These massive and bright BHs are likely to be heavily obscured in the rest-frame UV and thus are not selected as LRDs, due to the lack of a clear blue component.

### 5.2. Final Remarks

Using observed NIR colors to pick out active BHs in extragalactic fields is by no means a novel endeavor and has already been successfully done with the IRAC instrument on board the Spitzer Space Telescope (Lacy et al. 2004; Stern et al. 2005; Donley et al. 2012). This method, however, is still in its infancy when it comes to JWST (Labbé et al. 2023a; Andika et al. 2024). As already pointed out by Matthee et al. (2024), very few JWST programs that detect dusty AGN were actually designed with AGN in mind, implying that there is still more that we can do to address a growing number of questions about this population.

First, the physical mechanisms that govern BH formation and growth in these systems are still poorly understood, although there already exists a growing body of works that try to decipher this enigmatic population (Greene et al. 2024; Silk et al. 2024). One such puzzle is the origin of the blue light found in LRDs. The similarity between the blue slopes of low-metallicity star-forming galaxies and quasars does not allow us to make a clear assessment of whether the rest-UV light originates from the AGN itself or the compact host galaxy surrounding it, from the continuum alone. One way to solve this is to target the Mg II doublet ($\lambda_{rest} \sim 2800$ Å), the C IV, Si IV, or He II ($\lambda_{rest} \sim 1840$ Å) lines (e.g., see Maiolino et al. 2023) and confirm whether these are broadened or not. This, however, would require longer integration times with NIRSpec, as medium- or even high-resolution gratings would be required to achieve the necessary spectral fidelity. Moreover, while in principle the detection of broad UV emission lines could hint at the AGN being responsible for some UV light, this would not necessarily mean that the UV continuum also originates from the same source.

Second, there are no models as yet that can adequately describe the light we see emerging from these objects. So far, we have mainly had to rely on combinations of dust-free and dust-attenuated empirical models of local quasars, which might be adequately describing AGN at high-$z$. Moreover, the lingering uncertainty on the $A_V$ correction can introduce some biases into our estimates of $L_{bol}$ and the $M_{BH}$. One solution to alleviate this is to stack the spectra of known LRDs, to define sets of reliable models describing these populations and aiding with further photometric selection.

Third, it is crucial to note that a substantial proportion of massive SMBHs (with $M_{BH} > 10^8 M_\odot$) at high redshifts (high-$z$) can be heavily obscured, as implied by DELPHI. Similar conclusions were already reached from the X-ray luminosity functions at $z > 5$, both from simulations (Ni et al. 2020) and observations (Aird et al. 2015; Vito et al. 2018). In addition, Trebitsch et al. (2019) have shown that accreting SMBHs in Lyman-break galaxies are rarely UV-bright. With this in mind, selecting these massive AGN as LRDs would thus not be possible, as a combination of very deep rest-UV imaging and large areas are required. Despite that, these objects should still appear bright in the NIR, which opens up the possibility of effectively identifying them through large or parallel surveys using MIRI.

Finally, as has already recently been shown by Williams et al. (2023a) and Pérez-González et al. (2024), MIRI can also assist with clarifying the true numbers of AGN among LRDs, as some of these could be dusty progenitors of compact ellipticals.

Early results from JWST have already provided us with quite unexpected and remarkable results regarding the number densities of early AGN, leading to a shift in our understanding of their formation and growth in the early Universe. Our results highlight the potential of using NIRCam alone to select reddened AGN at high-$z$ in an effort to better understand their properties and abundance. While some limitations to this technique exist, as we have already discussed in our work, this provides a crucial set of next steps in order to bridge the gap between UV-bright quasars and faint SMBHs. However, it is already evident that the importance of faint, reddened AGN at early times cannot be overlooked.

## Acknowledgments

We thank the anonymous referee for a number of constructive suggestions, which helped to greatly improve the quality of this manuscript. We are grateful to Dale Kocevski and Kohei Inayoshi for their patience with helping us to spot and correct minor inconsistencies in the manuscript. The authors would like to thank Sarah Bosman for insightful discussions about UV-bright quasars at high redshift. We also thank Mauro Giavalisco, Hollis Akins, and Meghana Killi for useful discussions regarding the nature of dust-obscured AGN. V.K. and K.I.C. acknowledge funding from the Dutch Research Council (NWO) through the award of the Vici grant VI.C.212.036. J.E.G. acknowledges support from NSF/AAG grant #1007094 and also support from NSF/AAG grant #1007052. P.D. and M.T. acknowledge support from the NWO grant 016.VIDI.189.162 ("ODIN"). P.D. also acknowledges support from the European Commission's and University of Groningen's CO-FUND Rosalind Franklin program. T.B.M. was supported by a CIERA Postdoctoral Fellowship. This work is based on observations made with the NASA/ESA/CSA James Webb Space Telescope. The data were obtained from the Mikulski Archive for Space Telescopes at the Space Telescope Science Institute, which is operated by the Association of Universities for Research in Astronomy, Inc., under NASA contract NAS 5-03127 for JWST. All the JWST and HST data used in this paper can be found on MAST at doi:10.17909/de9v-7893. Some of the data products presented herein were retrieved from the Dawn JWST Archive (DJA). DJA is an initiative of the Cosmic Dawn Center, which is funded by the Danish National Research Foundation under grant No. 140. This work used computing resources provided by Northwestern University and the Center for Interdisciplinary Exploration and Research in Astrophysics (CIERA). This research was supported in part through the computational resources and staff contributions provided for the Quest high-performance computing facility at Northwestern University, which is jointly supported by the Office of the Provost, the Office for Research, and Northwestern University Information Technology.

*Facilities:* JWST, HST.

*Software:* EAZY (Brammer et al. 2008), FSPS (Conroy et al. 2009), pysersic (Pasha & Miller 2023), grizli (Brammer 2023), msaexp (Brammer 2022).

## Appendix

In this section we present a shortened example version of the table (Table 4) which lists the locations of our sources as well as all derived physical parameters.

**Table 4**
An Example of the Table Containing All Properties of Our Sources

| ID | Field | R.A. (deg) | Decl. (deg) | {filt}_flux ($\mu$Jy) | {filt}_fluxerr ($\mu$Jy) | $z_{\rm phot}$ | $A_{\rm V}$ (mag) | log ($L_{\rm bol}$/[erg s$^{-1}$]) | $M_{\rm UV}$ (ABmag) | $r_{\rm eff,pix}$ (pix) | $r_{\rm eff,phys}$ (pc) |
|---|---|---|---|---|---|---|---|---|---|---|---|
| 1381 | PRIMER-UDS | 34.440988 | −5.209337 | ⋯ | ⋯ | $5.66^{+0.03}_{-1.66}$ | $3.1 \pm 0.3$ | $45.0 \pm 0.1$ | $-17.52 \pm 0.3$ | <1.04 | <186 |
| 1470 | PRIMER-UDS | 34.260549 | −5.209163 | ⋯ | ⋯ | $5.40^{+0.06}_{-0.09}$ | $1.1 \pm 0.1$ | $44.4 \pm 0.2$ | $-18.45 \pm 0.1$ | <1.23 | <230 |
| 1544 | PRIMER-UDS | 34.377413 | −5.209023 | ⋯ | ⋯ | $5.46^{+0.02}_{-0.01}$ | $1.0 \pm 0.2$ | $44.5 \pm 0.4$ | $-18.84 \pm 0.1$ | <1.02 | <187 |
| 1939 | PRIMER-UDS | 34.403098 | −5.208186 | ⋯ | ⋯ | $4.36^{+0.17}_{-0.30}$ | $1.3 \pm 0.1$ | $44.6 \pm 0.4$ | $-17.78 \pm 0.1$ | <0.71 | <144 |
| 3992 | PRIMER-UDS | 34.367304 | −5.204196 | ⋯ | ⋯ | $5.66^{+0.02}_{-0.02}$ | $1.6 \pm 0.2$ | $45.2 \pm 0.2$ | $-18.53 \pm 0.1$ | <0.55 | <104 |
| 7991 | PRIMER-UDS | 34.293687 | −5.196477 | ⋯ | ⋯ | $5.66^{+1.38}_{-0.10}$ | $2.4 \pm 0.3$ | $45.9 \pm 0.4$ | $-18.47 \pm 0.3$ | <1.11 | <196 |
| 8559 | PRIMER-UDS | 34.465426 | −5.195333 | ⋯ | ⋯ | $7.94^{+0.09}_{-0.13}$ | $3.9 \pm 0.1$ | $46.7 \pm 0.2$ | $-19.50 \pm 0.1$ | <0.68 | <111 |
| 10404 | PRIMER-UDS | 34.462872 | −5.191960 | ⋯ | ⋯ | $5.66^{+0.03}_{-0.02}$ | $2.2 \pm 0.2$ | $45.6 \pm 0.3$ | $-18.13 \pm 0.1$ | <0.50 | <101 |
| 11219 | PRIMER-UDS | 34.471126 | −5.190444 | ⋯ | ⋯ | $5.43^{+0.03}_{-0.03}$ | $2.7 \pm 0.2$ | $45.9 \pm 0.3$ | $-19.20 \pm 0.1$ | <0.42 | <84 |
| 14419 | PRIMER-UDS | 34.399178 | −5.184323 | ⋯ | ⋯ | $4.82^{+0.27}_{-0.07}$ | $0.9 \pm 0.2$ | $44.5 \pm 0.3$ | $-17.84 \pm 0.1$ | <0.64 | <135 |
| 15257 | PRIMER-UDS | 34.431864 | −5.182780 | ⋯ | ⋯ | $6.92^{+0.06}_{-1.46}$ | $1.3 \pm 0.2$ | $45.2 \pm 0.1$ | $-18.85 \pm 0.2$ | <0.79 | <133 |
| 16999 | PRIMER-UDS | 34.508058 | −5.180084 | ⋯ | ⋯ | $4.21^{+0.15}_{-0.17}$ | $1.1 \pm 0.1$ | $45.2 \pm 0.2$ | $-18.41 \pm 0.1$ | <0.65 | <154 |
| 18804 | PRIMER-UDS | 34.363515 | −5.176964 | ⋯ | ⋯ | $4.32^{+0.07}_{-0.27}$ | $1.5 \pm 0.1$ | $45.1 \pm 0.4$ | $-19.21 \pm 0.1$ | <0.45 | <114 |
| 18892 | PRIMER-UDS | 34.268908 | −5.176722 | ⋯ | ⋯ | $4.73^{+0.04}_{-0.20}$ | $1.0 \pm 0.1$ | $44.4 \pm 0.2$ | $-17.34 \pm 0.1$ | <0.62 | <123 |
| 19416 | PRIMER-UDS | 34.460763 | −5.175813 | ⋯ | ⋯ | $5.43^{+0.04}_{-0.06}$ | $1.9 \pm 0.1$ | $44.8 \pm 0.3$ | $-18.32 \pm 0.1$ | <1.07 | <221 |
| 21108 | PRIMER-UDS | 34.362963 | −5.173200 | ⋯ | ⋯ | $7.14^{+1.8}_{-0.10}$ | $2.6 \pm 0.3$ | $45.8 \pm 0.2$ | $-18.09 \pm 0.3$ | <0.62 | <105 |
| 22773 | PRIMER-UDS | 34.438986 | −5.170543 | ⋯ | ⋯ | $4.40^{+0.21}_{-0.10}$ | $1.3 \pm 0.2$ | $44.7 \pm 0.2$ | $-18.88 \pm 0.1$ | <0.57 | <129 |
| 23575 | PRIMER-UDS | 34.408020 | −5.169147 | ⋯ | ⋯ | $5.66^{+0.02}_{-0.01}$ | $2.0 \pm 0.2$ | $45.1 \pm 0.3$ | $-18.20 \pm 0.1$ | <0.76 | <137 |
| 24081 | PRIMER-UDS | 34.346207 | −5.168197 | ⋯ | ⋯ | $5.66^{+0.02}_{-0.02}$ | $1.8 \pm 0.2$ | $45.1 \pm 0.3$ | $-18.42 \pm 0.1$ | <0.52 | <100 |

**Note.** A full version of this table is available on Zenodo at doi:10.5281/zenodo.10820724. The sizes are measured in the F444W band on the $0\farcs04$ images. The FWHM of the F444W PSF is 3.45 pixels.

## ORCID iDs

Vasily Kokorev https://orcid.org/0000-0002-5588-9156
Karina I. Caputi https://orcid.org/0000-0001-8183-1460
Jenny E. Greene https://orcid.org/0000-0002-5612-3427
Pratika Dayal https://orcid.org/0000-0001-8460-1564
Maxime Trebitsch https://orcid.org/0000-0002-6849-5375
Sam E. Cutler https://orcid.org/0000-0002-7031-2865
Seiji Fujimoto https://orcid.org/0000-0001-7201-5066
Ivo Labbé https://orcid.org/0000-0002-2057-5376
Tim B. Miller https://orcid.org/0000-0001-8367-6265
Edoardo Iani https://orcid.org/0000-0001-8386-3546
Rafael Navarro-Carrera https://orcid.org/0000-0001-6066-4624
Pierluigi Rinaldi https://orcid.org/0000-0002-5104-8245

## References

Adams, N. J., Conselice, C. J., Ferreira, L., et al. 2023, MNRAS, 518, 4755
Aird, J., Coil, A. L., Georgakakis, A., et al. 2015, MNRAS, 451, 1892
Akins, H. B., Casey, C. M., Allen, N., et al. 2023, ApJ, 956, 61
Andika, I. T., Jahnke, K., Onoue, M., et al. 2024, A&A, 685, A25
Atek, H., Chemerynska, I., Wang, B., et al. 2023, MNRAS, 524, 5486
Austin, D., Adams, N., Conselice, C. J., et al. 2023, ApJL, 952, L7
Baggen, J. F. W., van Dokkum, P., Labbé, I., et al. 2023, ApJL, 955, L12
Bagley, M. B., Finkelstein, S. L., Koekemoer, A. M., et al. 2023, ApJL, 946, L12
Bañados, E., Carilli, C., Walter, F., et al. 2018, ApJL, 861, L14
Banerji, M., Alaghband-Zadeh, S., Hewett, P. C., & McMahon, R. G. 2015, MNRAS, 447, 3368
Barbary, K. 2016, JOSS, 1, 58
Barro, G., Perez-Gonzalez, P. G., Kocevski, D. D., et al. 2024, ApJ, 963, 128
Behroozi, P., Conroy, C., Wechsler, R. H., et al. 2020, MNRAS, 499, 5702
Behroozi, P., Wechsler, R. H., Hearin, A. P., & Conroy, C. 2019, MNRAS, 488, 3143
Behroozi, P. S., & Silk, J. 2015, ApJ, 799, 32
Bertin, E., & Arnouts, S. 1996, A&AS, 117, 393
Bezanson, R., Labbe, I., Whitaker, K. E., et al. 2022, arXiv:2212.04026
Blanton, M. R., & Roweis, S. 2007, AJ, 133, 734
Bogdan, A., Goulding, A., Natarajan, P., et al. 2024, NatAs, 8, 126
Bouwens, R. J., Illingworth, G. D., Oesch, P. A., et al. 2015, ApJ, 803, 34
Bouwens, R. J., Oesch, P. A., Stefanon, M., et al. 2021, AJ, 162, 47
Boylan-Kolchin, M. 2023, NatAs, 7, 731
Bradley, L. D., Coe, D., Brammer, G., et al. 2023, ApJ, 955, 13
Brammer, G. 2022, msaexp: NIRSpec analyis tools v0.3, Zenodo, doi:10.5281/zenodo.7299500
Brammer, G. 2023, grizli v1.8.2, Zenodo, doi:10.5281/zenodo.7712834
Brammer, G. B., van Dokkum, P. G., & Coppi, P. 2008, ApJ, 686, 1503
Bunker, A. J., Saxena, A., Cameron, A. J., et al. 2023, A&A, 677, A88
Burgasser, A. J., Gerasimov, R., Bezanson, R., et al. 2024, ApJ, 962, 177
Carnall, A. C., Begley, R., McLeod, D. J., et al. 2023, MNRAS, 518, L45
Casey, C. M., Akins, H. B., Shuntov, M., et al. 2024, ApJ, 965, 98
Chabrier, G. 2003, PASP, 115, 763
Conroy, C., Gunn, J. E., & White, M. 2009, ApJ, 699, 486
Curtis-Lake, E., Carniani, S., Cameron, A., et al. 2023, NatAs, 7, 622
Davé, R., Anglés-Alcázar, D., Narayanan, D., et al. 2019, MNRAS, 486, 2827
Dayal, P., Choudhury, T. R., Bromm, V., & Pacucci, F. 2017, ApJ, 836, 16
Dayal, P., Ferrara, A., Dunlop, J. S., & Pacucci, F. 2014, MNRAS, 445, 2545
Dayal, P., Ferrara, A., Sommovigo, L., et al. 2022, MNRAS, 512, 989
Dayal, P., Rossi, E. M., Shiralilou, B., et al. 2019, MNRAS, 486, 2336
Dayal, P., Volonteri, M., Choudhury, T. R., et al. 2020, MNRAS, 495, 3065
Dayal, P., Volonteri, M., Greene, J. E., et al. 2024, arXiv:2401.11242
Donley, J. L., Koekemoer, A. M., Brusa, M., et al. 2012, ApJ, 748, 142
Eisenstein, D. J., Johnson, B. D., Robertson, B., et al. 2023a, arXiv:2310.12340
Eisenstein, D. J., Willott, C., Alberts, S., et al. 2023b, arXiv:2306.02465
Endsley, R., Stark, D. P., Lyu, J., et al. 2023, MNRAS, 520, 4609
Fan, X., Banados, E., & Simcoe, R. A. 2023, ARA&A, 61, 373
Ferrara, A., Pallottini, A., & Dayal, P. 2023, MNRAS, 522, 3986
Finkelstein, S. L., & Bagley, M. B. 2022, ApJ, 938, 25
Finkelstein, S. L., Leung, G. C. K., Bagley, M. B., et al. 2023, arXiv:2311.04279
Fruchter, A. S., & Hook, R. N. 2002, PASP, 114, 144
Fu, H., Isbell, J., Casey, C. M., et al. 2017, ApJ, 844, 123
Fujimoto, S., Bezanson, R., Labbe, I., et al. 2023a, arXiv:2309.07834
Fujimoto, S., Brammer, G. B., Watson, D., et al. 2022, Natur, 604, 261
Fujimoto, S., Kohno, K., Ouchi, M., et al. 2023b, arXiv:2303.01658
Fujimoto, S., Wang, B., Weaver, J., et al. 2023c, arXiv:2308.11609
Furtak, L. J., Labbé, I., Zitrin, A., et al. 2024, Natur, 628, 57
Furtak, L. J., Zitrin, A., Plat, A., et al. 2023a, ApJ, 952, 142
Furtak, L. J., Zitrin, A., Weaver, J. R., et al. 2023b, MNRAS, 523, 4568
Gaia Collaboration, Brown, A. G. A., Vallenari, A., et al. 2021, A&A, 649, A1
Gehrels, N. 1986, ApJ, 303, 336
Giallongo, E., Grazian, A., Fiore, F., et al. 2019, ApJ, 884, 19
Glikman, E., Helfand, D. J., & White, R. L. 2006, ApJ, 640, 579
Glikman, E., Simmons, B., Mailly, M., et al. 2015, ApJ, 806, 218
Gordon, K. D., Clayton, G. C., Misselt, K. A., Landolt, A. U., & Wolff, M. J. 2003, ApJ, 594, 279
Goulding, A. D., Greene, J. E., Setton, D. J., et al. 2023, ApJL, 955, L24
Grazian, A., Giallongo, E., Boutsia, K., et al. 2018, A&A, 613, A44
Greene, J. E., & Ho, L. C. 2005, ApJ, 630, 122
Greene, J. E., Labbe, I., Goulding, A. D., et al. 2024, ApJ, 964, 39
Harikane, Y., Zhang, Y., Nakajima, K., et al. 2023, ApJ, 959, 39
He, W., Akiyama, M., Enoki, M., et al. 2024, ApJ, 962, 152
Inayoshi, K., Visbal, E., & Haiman, Z. 2020, ARA&A, 58, 27
Jin, S., Sillassen, N. B., Magdis, G. E., et al. 2023, A&A, 670, L11
Kannan, R., Springel, V., Hernquist, L., et al. 2023, MNRAS, 524, 2594
Kartaltepe, J. S., Rose, C., Vanderhoof, B. N., et al. 2023, ApJL, 946, L15
Kashikawa, N., Ishizaki, Y., Willott, C. J., et al. 2015, ApJ, 798, 28
Kaspi, S., Smith, P. S., Netzer, H., et al. 2000, ApJ, 533, 631
Kato, N., Matsuoka, Y., Onoue, M., et al. 2020, PASJ, 72, 84
Killi, M., Watson, D., Brammer, G., et al. 2023, arXiv:2312.03065
Kocevski, D. D., Onoue, M., Inayoshi, K., et al. 2023, ApJL, 954, L4
Kokorev, V., Brammer, G., Fujimoto, S., et al. 2022, ApJS, 263, 38
Kokorev, V., Fujimoto, S., Labbe, I., et al. 2023a, ApJL, 957, L7
Kokorev, V., Jin, S., Magdis, G. E., et al. 2023b, ApJL, 945, L25
Kron, R. G. 1980, ApJS, 43, 305
Kulkarni, G., Worseck, G., & Hennawi, J. F. 2019, MNRAS, 488, 1035
Labbé, I., Greene, J. E., Bezanson, R., et al. 2023a, arXiv:2306.07320
Labbé, I., Oesch, P. A., Bouwens, R. J., et al. 2013, ApJL, 777, L19
Labbé, I., van Dokkum, P., Nelson, E., et al. 2023b, Natur, 616, 266
Lacy, M., Storrie-Lombardi, L. J., Sajina, A., et al. 2004, ApJS, 154, 166
Lambrides, E., Chiaberge, M., Long, A., et al. 2024, ApJL, 961, L25
Laporte, N., Bauer, F. E., Troncoso-Iribarren, P., et al. 2017, A&A, 604, A132
Larson, R. L., Finkelstein, S. L., Kocevski, D. D., et al. 2023, ApJL, 953, L29
Leung, G. C. K., Bagley, M. B., Finkelstein, S. L., et al. 2023, ApJL, 954, L46
Lovell, C. C., Harrison, I., Harikane, Y., Tacchella, S., & Wilkins, S. M. 2023, MNRAS, 518, 2511
Maiolino, R., Scholtz, J., Curtis-Lake, E., et al. 2024, Natur, 627, 59
Maiolino, R., Scholtz, J., Witstok, J., et al. 2023, arXiv:2305.12492
Marchesini, D., van Dokkum, P. G., Förster Schreiber, N. M., et al. 2009, ApJ, 701, 1765
Mason, C. A., Trenti, M., & Treu, T. 2023, MNRAS, 521, 497
Matsuoka, Y., Onoue, M., Iwasawa, K., et al. 2023, ApJL, 949, L42
Matsuoka, Y., Strauss, M. A., Kashikawa, N., et al. 2018, ApJ, 869, 150
Matthee, J., Naidu, R. P., Brammer, G., et al. 2024, ApJ, 963, 129
Mauerhofer, V., & Dayal, P. 2023, MNRAS, 526, 2196
Mitra, S., Choudhury, T. R., & Ferrara, A. 2018, MNRAS, 473, 1416
Morishita, T., Stiavelli, M., Trenti, M., et al. 2020, ApJ, 904, 50
Naidu, R. P., Oesch, P. A., van Dokkum, P., et al. 2022, ApJL, 940, L14
Ni, Y., Di Matteo, T., Gilli, R., et al. 2020, MNRAS, 495, 2135
Niida, M., Nagao, T., Ikeda, H., et al. 2020, ApJ, 904, 89
Oesch, P. A., Brammer, G., Naidu, R. P., et al. 2023, MNRAS, 525, 2864
Oke, J. B. 1974, ApJS, 27, 21
Ormerod, K., Conselice, C. J., Adams, N. J., et al. 2024, MNRAS, 527, 6110
Pacucci, F., Dayal, P., Harikane, Y., Inoue, A. K., & Loeb, A. 2022, MNRAS, 514, L6
Pacucci, F., Nguyen, B., Carniani, S., Maiolino, R., & Fan, X. 2023, ApJL, 957, L3
Pasha, I., & Miller, T. B. 2023, JOSS, 8, 5703
Pérez-González, P. G., Barro, G., Rieke, G. H., et al. 2024, arXiv:2401.08782
Piana, O., Dayal, P., & Choudhury, T. R. 2022, MNRAS, 510, 5661
Planck Collaboration, Aghanim, N., Akrami, Y., et al. 2020, A&A, 641, A6
Rigby, J., Perrin, M., McElwain, M., et al. 2023, PASP, 135, 048001
Robertson, B. E., Tacchella, S., Johnson, B. D., et al. 2023, NatAs, 7, 611
Rosas-Guevara, Y., Bower, R. G., Schaye, J., et al. 2016, MNRAS, 462, 190
Schechter, P. 1976, ApJ, 203, 297
Schmidt, M. 1968, ApJ, 151, 393

Scholtz, J., Maiolino, R., D'Eugenio, F., et al. 2023, arXiv:2311.18731
Sérsic, J. L. 1963, BAAA, 6, 41
Shen, X., Hopkins, P. F., Faucher-Giguère, C.-A., et al. 2020, MNRAS, 495, 3252
Silk, J., Begelman, M., Norman, C., Nusser, A., & Wyse, R. 2024, ApJL, 961, 39
Skelton, R. E., Whitaker, K. E., Momcheva, I. G., et al. 2014, ApJS, 214, 24
Steinhardt, C. L., Kokorev, V., Rusakov, V., Garcia, E., & Sneppen, A. 2023, ApJL, 951, L40
Stern, D., Eisenhardt, P., Gorjian, V., et al. 2005, ApJ, 631, 163
Sun, G., Faucher-Giguère, C.-A., Hayward, C. C., & Shen, X. 2023, MNRAS, 526, 2665
Trebitsch, M., Hutter, A., Dayal, P., et al. 2023, MNRAS, 518, 3576
Trebitsch, M., Volonteri, M., & Dubois, Y. 2019, MNRAS, 487, 819
Übler, H., Maiolino, R., Curtis-Lake, E., et al. 2023, A&A, 677, A145
Valentino, F., Brammer, G., Gould, K. M. L., et al. 2023, ApJ, 947, 20
Vanden Berk, D. E., Richards, G. T., Bauer, A., et al. 2001, AJ, 122, 549
Vito, F., Brandt, W. N., Yang, G., et al. 2018, MNRAS, 473, 2378
Volonteri, M., Reines, A. E., Atek, H., Stark, D. P., & Trebitsch, M. 2017, ApJ, 849, 155
Wang, B., Fujimoto, S., Labbe, I., et al. 2023, ApJL, 957, L34
Wang, L., Gao, F., Best, P. N., et al. 2021, A&A, 648, A8
Weaver, J. R., Cutler, S. E., Pan, R., et al. 2024, ApJS, 270, 7
Weaver, J. R., Kauffmann, O. B., Ilbert, O., et al. 2022, ApJS, 258, 11
Weaver, J. R., Zalesky, L., Kokorev, V., et al. 2023, ApJS, 269, 20
Whitaker, K. E., Ashas, M., Illingworth, G., et al. 2019, ApJS, 244, 16
Whitaker, K. E., Labbé, I., van Dokkum, P. G., et al. 2011, ApJ, 735, 86
Wilkins, S. M., Vijayan, A. P., Lovell, C. C., et al. 2022, MNRAS, 517, 3227
Williams, C. C., Alberts, S., Ji, Z., et al. 2023a, arXiv:2311.07483
Williams, H., Kelly, P. L., Chen, W., et al. 2023b, Sci, 380, 416
Yang, G., Caputi, K. I., Papovich, C., et al. 2023, ApJL, 950, L5
Yang, J., Wang, F., Fan, X., et al. 2021, ApJ, 923, 262
Yung, L. Y. A., Somerville, R. S., Finkelstein, S. L., Popping, G., & Davé, R. 2019, MNRAS, 483, 2983
Yung, L. Y. A., Somerville, R. S., Finkelstein, S. L., et al. 2020, MNRAS, 496, 4574